Tropomyosin 1-I/C co-ordinates kinesin-1 and dynein motors during *oskar* mRNA transport

Simone Heber[1†], Mark A. McClintock[2†], Bernd Simon[3], Janosch Hennig[3,4], Simon L. Bullock[2*], Anne Ephrussi[1*]

1 Developmental Biology Unit, European Molecular Biology Laboratory, 69117 Heidelberg, Germany

2 Division of Cell Biology, MRC Laboratory of Molecular Biology, Cambridge CB2 0QH, United Kingdom

3 Structural and Computational Biology Unit, European Molecular Biology Laboratory, 69117 Heidelberg, Germany

4 Biochemistry IV, Biophysical Chemistry, University of Bayreuth, 95447 Bayreuth, Germany

[†]These authors contributed equally to this work

*Correspondence: sbullock@mrc-lmb.cam.ac.uk, anne.ephrussi@embl.org

Abstract

Dynein and kinesin motors mediate long-range intracellular transport, translocating towards microtubule minus and plus ends, respectively. Cargoes often undergo bidirectional transport by binding to both motors simultaneously. However, it is not known how motor activities are coordinated in such circumstances. In *Drosophila*, sequential activities of the dynein-dynactin-BicD-Egalitarian (DDBE) complex and of kinesin-1 deliver *oskar* mRNA from nurse cells to the oocyte, and within the oocyte to the posterior pole. Here, through *in vitro* reconstitution, we show that Tm1-I/C, a Tropomyosin-1 isoform, links kinesin-1 in an inactive state to DDBE-associated *oskar* mRNA. NMR spectroscopy, small-angle X-ray scattering and structural modeling indicate that Tm1-I/C suppresses kinesin-1 activity by stabilizing its autoinhibited conformation, thus preventing a tug-of-war between the opposite polarity motors until kinesin-1 is activated in the oocyte. Our work reveals a novel strategy ensuring sequential activity of microtubule motors.

Introduction

Motor protein driven transport along cytoskeletal tracks is important for subcellular localization of many cargoes, including organelles, vesicles and RNAs. Whereas myosin motors transport cargoes on actin filaments[1], cytoplasmic dynein and kinesin motors are responsible for translocation along microtubules, driving minus-end-directed and plus-end-directed movements, respectively. The cargoes for these motors, however, often travel bidirectionally, requiring the coordinated activity of the two motor classes. For instance, in neurons, mRNAs[2,3] and mitochondria[4] are shuttled bidirectionally to ensure their constant supply to distal regions. Because dynein and kinesin motors are often simultaneously bound to the same cargo[5,6], their activities must be tightly coordinated to allow for efficient transport rather than a futile tug-of-war.

Individual motors appear to be in an autoinhibited state by default, with activation driven by binding of adaptor proteins and cargoes. For instance, dynein is activated by binding of dynactin and one of a number of coiled-coil containing activating adaptors[7,8,9,10,11]. In the case of mRNA transport in *Drosophila*, dynein uses Bicaudal-D (BicD) as the activating adaptor, which is linked to double-stranded mRNA localization signals by the RNA-binding protein Egalitarian (Egl)[12,13]. Interaction of Egl and BicD with each other, as well as with the motor are enhanced by binding the mRNA signal, revealing a role for the mRNA in controlling motor activity[12,13,14,15].

Kinesin-1 is a tetramer consisting of two Kinesin heavy chains (Khc) and two Kinesin light chains (Klc)[16]. Khc contains an N-terminal globular motor domain, a coiled-coil stalk domain and a C-terminal disordered tail domain (Figure 1a) and is autoinhibited by folding of the tail region of the heavy chain back on its motor domain. This interaction has been proposed to involve pivoting of the coiled-coil stalk at a hinge region, which allows docking of a conserved isoleucine-alanine-lysine (IAK) motif in the tail onto the motor domain, thereby locking the complex in a conformation that prevents processive movement[17,18,19,20]. The autoinhibited conformation is stabilized by Klc[21,22], which binds to the Khc stalk domain[23,24] and is important for recognition of a range of cargoes[25].

However, the mechanisms of regulation in dual motor transport remain elusive, with only a small number of adaptor proteins that coordinate both motors having been reported. For example, the mitochondrial transport adaptor TRAK2 forms a complex with both kinesin-1 and dynein-dynactin and links these two motors functionally[26,27]. UNC-16, the *C. elegans* homolog of the lysosome adaptor JIP3/Syd, was also shown to link kinesin-1 and dynein, allowing for

plus-end-directed transport of dynein by kinesin-1[28,29]. Similarly, the dynein adaptor Hook3 can activate and link KIF1C (a kinesin-3 motor) and dynein[30,31].

oskar (*osk*) mRNA localization in the *Drosophila* egg chamber is a paradigm for the study of RNA transport and motor regulation. Motor-based delivery of *osk* to the posterior pole of the developing oocyte drives abdominal patterning and germline formation in the embryo[32]. Trafficking of *osk* mRNA to this site is mediated by the successive activities of the dynein[33] and kinesin-1[34.35] motors, and requires motor switching. In the germline syncytium, the oocyte is transcriptionally quiescent and relies on mRNAs provided by the 15 interconnected nurse cells for its development[36]. At this stage, microtubule minus ends are nucleated in the oocyte and extend into the nurse cells. Upon transcription in the nurse cells, *osk* mRNA is transported along the polarized microtubule cytoskeleton into the oocyte by dynein in complex with dynactin, BicD and Egl[12,33,37]. During mid-oogenesis, polarity of the microtubule cytoskeleton changes dramatically, with microtubule plus ends becoming enriched at the oocyte posterior. At this point, Khc translocates *osk* to the posterior pole[38]. Khc was previously shown to function in *Drosophila* oocytes largely independently of Klc[39,40], raising the question of how Khc is linked to *osk* and how motor activity is regulated.

Kinesin-mediated transport of *osk* RNA requires the unique I/C isoform of tropomyosin-1, Tm1-I/C (hereafter referred to as Tm1)[39,40,41,42]. Tm1 binds to a non-canonical but conserved cargo binding region in the Khc tail and stabilizes the interaction of the motor with RNA, suggesting a function as an adaptor[43]. Both Khc and Tm1 are already loaded onto the *osk* ribonucleoprotein particle (RNP) shortly after nuclear export in the nurse cells, although the motor only appears to become active in the oocyte during mid-oogenesis[42]. Similarly, dynein remains associated with *osk* RNPs during Khc-mediated transport within the oocyte, but is inactivated by displacement of Egl by the Staufen (Stau) protein[44,45].

How the two motors are linked simultaneously to *osk* RNPs, and how cargo-bound Khc is inhibited during dynein-mediated transport into the oocyte has been unclear. Here, we show that Tm1 inhibits Khc activity by stabilizing its autoinhibited conformation through a novel mechanism involving the regulatory tail domain. In addition, Tm1 links Khc to the dynein-transported *osk* RNP, thereby allowing co-transport of inactive Khc on *osk* RNA by dynein. *In vivo*, such a mechanism would avoid a tug-of-war between the two motors during the dynein-dependent delivery of *osk* RNPs to the oocyte whilst ensuring that Khc is available on these structures when it is time for this motor to move the RNPs to the posterior of the oocyte. With its cargo-binding and motor regulatory functions, we propose that Tm1 functions as a non-canonical light chain for kinesin-1 in the *Drosophila* oocyte.

Results

Tm1 can transport RNA with Khc *in vitro* but impairs Khc motility

In order to test the ability of Khc, Tm1 and the Khc-Tm1 complex to transport RNA, we performed total internal reflection fluorescence (TIRF) microscopy-based *in vitro* motility assays[15] using fluorescently labeled versions of recombinant, full-length Khc (Khc FL), full-length Tm1 (Tm1 FL) (Figure 1a, b) and *in vitro* transcribed *osk* 3'UTR RNA. At concentrations that allowed single-particle tracking (6.25 nM of each component), we observed transport of *osk* by Khc along microtubules in both the presence and absence of Tm1, albeit at low frequency (Figure 1c). In the absence of Tm1, 4.8 % (4/84) of Khc transport events co-localized with the *osk* 3'UTR signal. This value did not change significantly in the presence of Tm1 (2.8 %, 1/36; Figure 1d), despite 55 % (20/36) of Khc signals co-localizing with Tm1 signals. Correcting for the efficiency of labeling of Tm1 with the fluorophore (57 %) indicated that ~95 % of microtubule-bound Khc molecules were bound to Tm1. The high occupancy of Khc with Tm1 in these experiments is consistent with the strong binding between their interacting domains observed previously[43]. Mass photometry confirmed high occupancy of Khc with Tm1 at nanomolar concentrations (Figure S1), as well as the proposed 2:1 stoichiometry of the Khc-Tm1 complex[43]. We conclude from these experiments that Khc can associate with *osk* RNA but that the Khc-Tm1 complex does not have substantially higher affinity for the transcript in our assay conditions.

We next examined the effect of Tm1 on Khc motility. Without Tm1 present in the assay, microtubule-associated Khc complexes moved with a mean velocity of 0.221 μm s^{-1}. In the presence of Tm1, the mean velocity of Khc runs reduced to 0.068 μm s^{-1} (Figure 1e). These data reveal an inhibitory effect of Tm1 on Khc motility.

In addition to the 3'UTR, an RNA structure in the *osk* coding sequence, which is called the spliced *oskar* localization element (SOLE), is important for Khc-mediated transport of *osk in vivo*[46,47]. We tested if an RNA including the SOLE could stimulate motility of Khc in the presence of Tm1 by replacing the *osk* 3'UTR in our assay with a 135-nt RNA (*osk* min) comprising the SOLE and the oocyte entry signal of *osk* (Figure S2a), which resides in the 3'UTR and promotes dynein-mediated transport[48]. The inhibitory effect of Tm1 on Khc motility was also observed in the presence of *osk* min (Figure S2b-f). Thus, Tm1 inhibits motility of Khc in both the presence and absence of the SOLE element.

Tm1 inhibits Khc motility via the Khc regulatory tail

In order to elucidate the molecular mechanism behind Tm1-mediated inhibition of Khc, we set out to identify the region of Khc that is involved in this process. Regulatory functions have been attributed to an auxiliary, ATP-independent microtubule-binding domain (AMB) and the autoinhibitory IAK motif within the Khc tail (Figure 1a)[19,49,50]. Whereas the AMB allows for microtubule-sliding by Khc[51], the IAK motif inhibits Khc's ATPase activity[17,19], and thus processive motility, by binding to the Khc motor domain and locking the two Khc heads in a conformation that prevents neck-linker undocking and ADP-release[18]. We tested whether the regulatory tail is responsible for Tm1-mediated inhibition of Khc by assessing the effect of Tm1 on the motility of a tailless Khc truncation (Khc910; Figure 2a). As expected of a Khc without its regulatory tail, Khc910 was hyperactive in the *in vitro* motility assay, exhibiting more processive runs (Figure 2c and Table S1), an increased likelihood of processive movement upon binding microtubules (Figure 2d), and faster motility (Figure 2e and Table S1) than the full-length motor complex. However, the presence of Tm1 did not inhibit Khc910 motility (Figure 2c-e and Table S1). The same effects were observed when experiments were performed with *osk* min instead of *osk* 3'UTR (Figure S2c-f). These observations demonstrate that the regulatory tail of Khc is required for Tm1-mediated inhibition of motility.

To assess the relevance of the autoinhibitory IAK motif in the Khc tail for Tm1-mediated inhibition, we deleted this feature whilst leaving the AMB intact. To this end, we produced Khc940, which is truncated C-terminal to the AMB domain. Khc940 was hyperactive (in terms of the number of processive runs, fraction of Khc binding events that resulted in processive motility, and velocity) to a degree comparable to that of Khc910 (Figure 2b-e). However, despite the fact that a smaller fraction of Khc940 co-localized with Tm1 as compared with Khc FL and Khc910 (Figure S3), Khc940 was sensitive to inhibition by Tm1, as the number of runs, fraction of processive Khc, and Khc velocities were reduced in its presence (Figure 2b-e and Table S1). We conclude that Khc inhibition by Tm1 does not depend on the IAK motif and therefore involves another region of the Khc tail.

Khc inhibition by Tm1 is mediated by the Khc AMB domain

To test if the AMB domain in the Khc tail is required for inhibition by Tm1, we produced a Khc mutant in which only the AMB domain (aa 911-938) was deleted (KhcΔAMB) and tested its motility with and without Tm1 (Figure 3a). KhcΔAMB did not have an increased frequency or likelihood of processive movement or higher velocity compared to Khc FL (Figure 3b-d and Table S2), indicating that autoinhibition is not disrupted in this protein. Strikingly, the frequency, likelihood of motility, and velocity of processive KhcΔAMB movements were not decreased by Tm1 (Figure 3a-d and Table S2), despite the proportion of complexes associated with Tm1

171 not differing significantly from what was observed for Khc FL or Khc910 (Figure S4). Taken
172 together, these results reveal that the AMB domain of Khc mediates inhibition by Tm1 but is
173 not necessary for Tm1 binding.

174 The N-terminal domain of Tm1 is required for its inhibitory function

175 We next investigated which features of Tm1 mediate Khc inhibition. We previously showed
176 that a truncated Tm1 protein (1-335 of the 441-amino-acid full-length protein) comprising the
177 disordered N-terminal domain and the minimal Khc-binding region of the coiled-coil domain
178 can suppress *osk* RNA mislocalization in *Drosophila* oocytes that lack the endogenous Tm1
179 protein[43]. We therefore compared the effect of Tm1 1-335 to Tm1 FL in the motility assay
180 (Figure 4a) and found that both proteins inhibit Khc motility to a similar extent (Figure 4b-d
181 and Table S3). We also observed that the fraction of Tm1-bound Khc did not differ significantly
182 between Tm1 1-335 and Tm1 FL (Figure S5). These data show that the N-terminal region of
183 Tm1 is sufficient to inhibit Khc.
184
185 To address whether the Khc-binding domain of Tm1 (aa 252-334) is also sufficient to produce
186 an inhibitory effect we performed motility assays with this protein. We compared the effects of
187 untagged, unlabeled Tm1 FL and Tm1 252-334 (Figure 4e) on Khc motility. Whereas Tm1 FL
188 again decreased the number of processive runs of Khc, we observed no negative effect of
189 Tm1 252-334 on motility (Figure 4e, f, Figure S5d-f and Table S3). These results suggest that
190 inhibition of Khc requires the unstructured, N-terminal domain of Tm1.

191 Tm1 binding affects the disordered region of the regulatory Khc tail

192 Next, we set out to better understand the molecular mechanism of Khc inhibition by Tm1.
193 Because the inhibitory effect of Tm1 is mediated by the auxiliary microtubule-binding region
194 (AMB) within the Khc tail, we reasoned that Tm1 could alter microtubule binding by the tail
195 domain, perhaps by providing an additional interaction with microtubules. In order to test this
196 notion, we performed microtubule-binding assays[52] with recombinant Tm1 proteins. Tm1 was
197 incubated with polymerized microtubules before pelleting of microtubules, together with bound
198 protein, by ultracentrifugation. As a positive control, we confirmed that both Khc FL and Khc
199 tail partially partitioned into the microtubule-containing pellet fraction (Figure S6a). A small
200 fraction of Tm1 1-335 also partitioned into the pellet, indicating that the N-terminal or coiled-
201 coil domain of Tm1 can interact with microtubules. However, we did not observe increased
202 partitioning of the Khc tail (Khc 855-975) into the microtubule fraction in the presence of Tm1
203 1-335 (Figure S6b). This observation indicates that association with Tm1 does not alter the
204 degree of binding of the Khc tail to microtubules.
205 In the crystal structure of the Khc tail bound to Tm1, the Khc coiled coil extends into the AMB
206 domain (last visible aa: 916)[43]. Attempts to crystallize the same Khc construct alone were

207 unsuccessful, raising the possibility that the isolated motor protein is more flexible. It is
208 conceivable that the extended coiled coil of Khc is induced upon Tm1 binding, which could
209 reduce flexibility of the tail, potentially locking it in a conformation that impairs Khc activity. To
210 test this hypothesis, we probed the structure of the Khc alternative cargo-binding domain and
211 tail (Khc 855-975) in solution by NMR spectroscopy. The ^{1}H,^{15}N-HSQC NMR spectrum of the
212 Khc tail showed 34 resonances, each corresponding to a backbone N-H correlation (Figure
213 5a). Backbone assignment experiments and resulting secondary chemical shifts revealed that
214 the visible peaks are disordered and correspond to aa 937-975, the very C-terminal part of the
215 Khc tail that contains the auto-inhibitory IAK motif. For all tested coiled-coil constructs of Khc,
216 resonances for aa 855-936 were broadened beyond detection due to short transversal
217 relaxation times. The unfavorable relaxation behavior of H-N resonances in coiled-coil
218 structures is caused by slow rotational tumbling of the axis perpendicular to the helix
219 orientation which is, in the case of Khc-Tm1, potentially further slowed down by transient
220 intermolecular oligomerization. The absence of resonances for aa 855-936 is thus consistent
221 with this entire part of the protein forming an extended coiled-coil structure, even in the
222 absence of Tm1. Our data therefore suggest that the AMB domain is part of the structured
223 coiled coil even in absence of Tm1.
224
225 To further investigate the effect of Tm1-binding on the disordered tail, we performed NMR
226 titration experiments to detect any effects of Tm1 binding on the tail region. Upon titration of
227 increasing amounts of Tm1, there were intensity decreases for several resonances in ^{1}H,^{15}N-
228 HSQC spectra of Khc 855-975 (Figure 5b, c). The affected residues correspond to the IAK
229 motif and its flanking regions. This effect could be observed both in the absence and presence
230 of a U10 RNA (Figure 5c, d), and depended on the N-terminal domain of Tm1 because the
231 Tm1 coiled-coil (aa 252-334) construct did not affect the spectra (Figure 5e). These findings
232 are in agreement with our earlier findings that Tm1 inhibits Khc motility in the absence of RNA
233 and that the N-terminal region of Tm1 is required for its inhibitory effect. These intensity
234 decreases for the IAK motif and its proximal residues indicate an induced conformational
235 change or a second, transient interaction of the Tm1 N-terminal domain with this region.

236 Tm1 does not affect the interaction of the Khc tail with the isolated Khc 237 motor domain

238 The above results led us to hypothesize that Tm1, upon binding to the coiled coil of Khc that
239 includes the AMB domain, influences the interaction of the Khc tail and motor domains. To test
240 this notion, we performed NMR titration experiments in which the Khc motor domain (aa Khc
241 1-365) was added to the tail domain prior to Tm1 1-335 titration. Titration of Khc 1-365 to
242 Khc 855-975 caused intensity losses for several resonances. As expected, the resonances
243 corresponding to the IAK motif (aa 941-948), as well as its flanking residues (aa 936-962),

were affected (Figure 5f, g). Some resonances in this region also showed chemical shift perturbations (Figure 5f, h). Taken together, these data confirm an interaction between Khc 855-975 (tail) and Khc 1-365 (motor). Additional titration of Tm1 1-335 to this Khc tail-motor complex caused further intensity decreases of the same resonances (Figure 5f, g), showing that Tm1 1-335 can bind to the Khc tail when it is associated with the motor domains. We conclude that binding of the Khc tail to Tm1 and the Khc motor are not mutually exclusive.

We therefore tested whether Tm1 can directly affect the interaction of the Khc motor and tail domains in GST-pulldown assays (Figure S7). When used as bait, the GST-tagged Khc tail domain (Khc 855-975) simultaneously captured the Khc motor domain (Khc 1-365) and Tm1 1-335, consistent with our NMR-based evidence that formation of a trimeric complex is possible. However, the fractions of Khc 1-365 and Tm1 1-335 pulled down by GST-Khc 855-975 were low, indicating a rather weak or transient interaction. Upon titration of Tm1 1-335, the amount of motor domain associating with the tail domain was not affected. Thus, we conclude that Tm1 does not alter the ability of the isolated Khc motor domain to interact with the isolated Khc tail domain.

Tm1 alters the auto-inhibited conformation of Khc

We next reasoned that Tm1 binding might stabilize the autoinhibited conformation of the full-length Khc by favoring additional interactions within the coiled-coil stalk domain, likely including the AMB domain. In order to obtain information about Khc's predominant conformation in its free and Tm1-bound states, we measured small-angle X-ray scattering (SAXS) of Khc and the Khc-Tm1 complex (Figure 6a). A dimensionless Kratky plot[53,54] of both scattering profiles (Figure 6b) shows that Khc and Khc-Tm1 are extended molecules with flexible elements. To identify structures that can explain the scattering curves of Khc and Khc-Tm1, we generated a large pool of Khc and Khc-Tm1 models by connecting coordinates of the structured parts that were generated by AlphaFold2[55,56]. Based on AlphaFold2 predictions, the Khc stalk contains four coiled-coil regions (cc 1-4) connected by flexible hinge regions (hinges 2-4). The stalk is connected to the motor domain's neck coiled coil by another flexible region (hinge 1) (Figure S8a) We subsequently randomized the connecting linker and tail regions to create a large pool of possible structures. In a second step, the C-terminal tail of one chain was pulled into the binding pocket of the motor domain resulting in a second pool of structures with random orientation of the stalk region and the IAK peptide bound to the motor domain dimer. Both pools of structures were sorted by the quality of the fit to the SAXS data.

For both Khc and the Khc-Tm1 complex, the structures with the lowest χ^2 values (i.e. best quality fits) all exhibited compact conformations with considerably lower than average values for the radius of gyration (*Rg*). Since the autoinhibited conformations were more compact than

281 the initial pool with randomized linker conformations, there were on average more structures
282 with low χ^2 values in the pools of structures with the IAK motif bound to the motor domains
283 (Figure S8b). Inspection of the structural models that best fit the scattering curves indicated
284 that the arrangement of the coiled-coils is different for Khc and Khc-Tm1. Looking at the angles
285 (Figure 6c-d) of consecutive coiled-coil regions of Khc models, we observed that the
286 conformation of the hinge regions (hinge 2: aa 586-603, hinge 3: aa 707-710 and hinge 4:
287 aa 839-843, Figure S8a) leads to bent structures of the coiled-coil regions cc1-cc2 and cc3-
288 cc4 and elongated cc2-cc3 orientation, resulting in a triangular shape of the molecule (Figure
289 6c, Figure S8d). In this conformation, the N- and C-terminal parts of the stalk are separated,
290 and the AMB domain, which mediates inhibition by Tm1, is not in proximity to other stalk
291 regions (Figure 6c, Figure S8d-e). For Khc-Tm1, the stalk folds at hinge 3 (Figure 6c, Figure
292 S8d), bringing N- and C-terminal halves of the stalk in proximity, with the AMB domain oriented
293 parallel to the N-terminal stalk region (Figure S8f). Fits with single models are a crude
294 approximation because in solution, Khc likely is in a dynamic equilibrium of a multitude of
295 autoinhibited and more open conformations. Nevertheless, such single models reflect a
296 possible predominant or average conformation of the protein. These data therefore suggest
297 that binding of Tm1 to Khc results in a shift of the conformational equilibrium towards different,
298 more compact structures of the Khc stalk domain. The autoinhibited conformation of Khc is
299 likely stabilized by interactions within the Tm1-bound stalk in addition to the motor-tail
300 interaction. This is in agreement with our findings that the Khc AMB domain in complex with
301 Tm1 can inhibit Khc independently of the IAK motif.

302 Tm1 links inactive Khc to dynein RNPs for minus-end-directed *osk* 303 transport

304 Khc and Tm1 are loaded onto *osk* RNPs in nurse cells prior to dynein-driven transport into the
305 oocyte[42]. We reasoned that during this process, enhanced inhibition of Khc by Tm1 would
306 favor minus-end-directed movement by preventing a tug-of-war between dynein and Khc that
307 could result in counterproductive movements of RNPs away from the oocyte. To assess if this
308 is the case, we set out to reconstitute *osk* RNPs containing Khc, Tm1 and dynein *in vitro*.
309
310 Since dynein and kinesin require different conditions for optimal motility, we used a modified
311 assay buffer that allows movement of both motor classes[58]. To exclude the possibility that Tm1
312 promotes minus-end-directed movement of *osk* RNPs by stimulating dynein activity directly,
313 we first assessed its effects on the motile properties of the minimal machinery for dynein-
314 mediated RNA transport (dynein, dynactin, BicD, Egalitarian (DDBE)) assembled with an *osk*
315 3'UTR fragment that is sufficient to initiate dynein movement *in vivo* (*osk* 3'UTR 2+3)[48]. While
316 Tm1 could be observed translocating with dynein and the *osk* RNA (Figure 7a), its presence
317 did not alter dynein velocity or run length on microtubules (Figure 7b, c and Table S4).

318 Furthermore, Tm1 had no effect on the percentage of microtubule-bound dyneins that undergo
319 directed motility or the frequency of dynein binding to microtubules or initiating transport along
320 them (Figure S9a-c and Table S4). Thus, Tm1 does not directly affect dynein motility.
321 Treatment of these reconstituted RNPs with RNase A after assembly dramatically reduced the
322 incidence of Tm1 association with DDBE-*osk* 3'UTR 2+3 (Figure 7d, e), indicating that Tm1 is
323 linked to the dynein machinery via *osk* RNA rather than through protein-protein interactions.
324 This observation is consistent with the finding that Tm1 does not directly influence DDBE
325 activity.
326
327 We next assessed the behavior of Khc in the presence of DDBE-*osk* 3'UTR 2+3 RNPs but
328 without Tm1. In these conditions, dynein and associated *osk* RNA exhibited long movements
329 toward the minus ends of microtubules (Figure 8a), as shown by polarity marking of the tracks
330 (Figure S10). Of the relatively few Khc runs that were observed, only ~25 % were directed
331 towards the microtubule plus end and those were seldomly associated with *osk* RNA (Figure
332 8a-c and Table S5). The remainder moved towards the minus end in association with dynein
333 and the RNA (Figure 8a-c), indicating some capacity of Khc to associate with DDBE-*osk* RNA
334 complexes. Khc in these complexes appeared to retain some activity, demonstrated by
335 occasional plus-end-directed movements after dissociating from DDBE-*osk* RNPs
336 translocating in the minus end direction (9/127 complexes, 7.1 %; Figure S11). Inclusion of
337 Tm1 in the assay caused a 12-fold increase in the incidence of minus-end-directed Khc
338 transport events (Figure 8a, b and Table S5), which overlapped with dynein and *osk* RNA
339 signals (Figure 8c). These data reveal that Tm1 promotes formation of dual-motor *osk* RNPs
340 in which dynein activity is dominant over that of kinesin, resulting in an overwhelming minus-
341 end-directed bias in Khc movement. Treatment of these *osk* RNPs with RNase A strongly
342 suppressed the Tm1-induced association of Khc with minus-end-directed DDBE-
343 *osk* 3'UTR 2+3 RNA complexes (Figure S12), supporting the notion that Tm1 achieves this
344 effect through interactions with *osk* RNA.
345
346 To determine if Tm1 additionally suppresses the activity of Khc within minus-end-directed
347 DDBE-*osk* RNPs, we compared dynein velocities and the distances traveled by Khc
348 toward microtubule minus ends in the presence and absence of Tm1. Consistent with an
349 inhibitory effect on Khc activity, Khc-bound DDBE-*osk* RNA complexes moved ~50 %
350 more rapidly towards the minus end in the presence of Tm1 (Figure 8d and Table S5).
351 Moreover, Tm1 allowed Khc to associate with minus-end-directed DDBE-*osk* RNA
352 complexes for distances on microtubules that were ~65 % greater than in its absence
353 (Figure 8e and Table S5), and significantly reduced the incidence of Khc directional
354 switches (6/848 complexes, 0.7 %; $p<0.0001$ compared to in the absence of Tm1 (Fisher's
355 exact test)). These observations suggest that Tm1 limits engagements of Khc with

356 microtubules that counter minus-end-directed motion. Collectively, these results support a
357 model in which Tm1 recruits Khc to the DDBE-*osk* complex in an inactive state thus avoiding
358 a tug-of-war between the opposite polarity motors.

Discussion

Tm1-I/C, an atypical RNA-binding isoform of tropomyosin 1, was recently implicated as an RNA adaptor for kinesin-1 transport[41,42]. By interacting directly with Khc's cargo-binding domain, Tm1 was shown to enhance RNA binding by Khc[43]. Our current study has revealed a previously unknown role of Tm1 in *osk* mRNP transport. We show that Tm1 negatively regulates Khc activity, which we propose occurs by inducing a conformational change in the Khc stalk domain that stabilizes the inhibitory Khc motor-tail interaction (Figure 9a). We demonstrate that Tm1 also links Khc in an inactive state to the dynein transport machinery. This work involves the first reconstitution of a native cargo-adaptor-motor complex that recapitulates regulation of both dynein and kinesin motors. *In vivo*, the mechanism we uncover would allow dynein-mediated transport of *osk* RNPs from the nurse cells to the oocyte to proceed without a tug-of-war with Khc whilst positioning the plus-end-directed motor on the RNPs for when it needs to drive their posteriorward movement within the mid-oogenesis oocyte (Figure 9b).

Kinesin-1 autoinhibition mechanisms

Despite decades of research, kinesin-1 autoinhibition is not fully understood. This is due in part to a paucity of structural information for full length kinesin-1. Whereas crystal structures of kinesin motor domains in different states are available, the conformations of the coiled-coil stalk in both the active and autoinhibited state of the motor remain elusive. While an extended conformation of the coiled-coil stalk was proposed to exist in active kinesin-1[59], this notion was challenged by subsequent studies that indicated an at least partially folded structure of the tail within the active complex[21,60]. A recent study involving structure prediction and single-particle negative stain electron microscopy questions if folding occurs at the flexible hinge region 2 and suggests a different conformation for the Khc stalk[61].

It has been proposed that the interaction of the IAK motif within the tail with the motor domain plays a key role in kinesin-1 autoinhibition. Consistent with this notion, we observed hyperactivity of *Drosophila* Khc motility when the IAK motif was deleted. However, it was recently shown that Klc inhibits Khc activity independently of the IAK-motor interaction[22]. We also find that the IAK motif is not needed for inhibition of Khc by Tm1. Instead, we find that the Khc AMB domain, a region outside the IAK motif previously shown to be essential for *osk* mRNA localization[62], contributes to inhibition in Khc-Tm1 complexes. Our work therefore identifies a novel role for the AMB domain.

Using NMR spectroscopy, we show that the IAK-motor interaction does not interfere with binding of regulating factors such as Tm1. Our SAXS data-driven structure modeling provides

396 insights into possible conformations of a full length kinesin-1. The Khc stalk adopts different
397 conformations when in complex with Tm1 (Figure 6c, d). This could explain why the IAK-motor
398 domain interaction, despite being necessary for autoinhibition, is insufficient to fully inhibit Khc.
399 It is conceivable that additional interactions in the rearranged, Tm1-bound stalk regions are
400 required to maintain the autoinhibited, folded conformation. This is in line with our own and
401 previous observations that the IAK-motor domain interaction is rather weak[17] and the report in
402 a recent preprint that interactions within the coiled-coil stalk and between stalk and motor
403 contribute to kinesin-1 autoinhibition[63]. Presumably, binding of Tm1 drives structural
404 rearrangements of the stalk that compact the molecule and stabilize the autoinhibited
405 conformation to robustly shut down Khc motility. We propose a model in which several weak
406 interactions – the motor-IAK interaction and interactions within the Tm1-bound coiled-coil stalk,
407 including the AMB domain – act synergistically to achieve this stable inhibited conformation of
408 Khc *in vivo* (Figure 9a).
409
410 With its functions in cargo-binding and motor regulation, we speculate that Tm1 acts as an
411 alternative Klc in the *Drosophila* germline to regulate processes which were previously thought
412 not to require a Klc[40]. Previously, PAT1 was shown to act as a positive regulator of Khc and
413 have redundant functions with Klc in the *Drosophila* germline [39]. As correct RNA localization
414 during oogenesis is critical for development, positive regulators such as PAT1 and negative
415 regulators such as Tm1 may have replaced Klc in order to provide nuanced regulation of Khc
416 activity. In the future, it will be interesting to determine whether Klc is also dispensable in other
417 tissues that use Tm1 for RNA localization, including the follicle cells of the egg chamber[64] and
418 the larval neuromuscular junction[65].
419

420 Co-ordination of kinesin-1 and dynein motors on *osk* RNPs

421 Although many cargo types have been shown to be transported by the action of dynein and
422 kinesin-1 motors, the mechanisms of motor regulation in the context of dual motor transport
423 have been elusive. We have identified one of very few known examples of a factor that links
424 dynein and kinesin-mediated transport. Furthermore, to our knowledge, Tm1 is the first
425 example of a protein that modulates dynein and kinesin behavior in a reconstituted dual-motor
426 assembly on a native cargo.
427
428 Several studies have reported that active dynein and kinesin motors engage in a tug-of-war
429 when artificially coupled[66,67,68,69,70,71]. However, the relevance of such mechanical antagonism
430 in localizing physiological cargoes for these motors is unresolved[6]. Although we also observe
431 motor opposition in reconstituted RNPs containing DDBE and Khc, our observation that Tm1
432 supports efficient dynein-mediated RNA localization through robust inhibition of Khc highlights

433 the importance of regulatory factors in addition to mechanical coupling in cargo-adaptor-motor
434 complexes.
435
436 Despite the potential for antagonistic engagement of dynein and kinesin on shared cargoes,
437 the motors can exhibit a puzzling co-dependence, in which strongly impairing the activity of
438 one motor type can inhibit the activity of the other[6]. Nonetheless, enhanced inhibition of Khc
439 by Tm1 in our reconstituted RNPs demonstrates the importance of negative kinesin regulation
440 in enabling robust dynein activity. Supporting the *in vivo* relevance of this regulatory logic,
441 kinesin-1 activating IAK mutations were recently shown to impair dynein-mediated transport
442 processes in *Aspergillus nidulans*[72]. Collectively, these observations point to complex interplay
443 between opposite polarity microtubule motors during bidirectional transport. Further
444 reconstitutions of dual-motor systems on native cargoes should reveal generalities of dynein-
445 kinesin crosstalk, as well as any cargo-specific mechanisms.
446

447 Potential kinesin-1 activation mechanisms in the female germline

448 Our study provides mechanistic insight into two critical aspects of *osk* mRNA transport – the
449 assembly of the dual motor complex and how Khc activity is suppressed during dynein-
450 mediated delivery of the transcript from the nurse cells to the oocyte. However, it is not known
451 how Tm1-mediated inhibition of Khc is alleviated at later stages of oogenesis in the oocyte.
452 One candidate to fulfill this role is Ensconsin. This protein is required for posterior *osk*
453 localization[73], as well as organelle transport in *Drosophila* neurons[74] and is homologous to
454 MAP7, which was recently shown to be required for full activity of the human kinesin-1 complex
455 *in vitro*[22,75]. Other factors that may relieve Khc inhibition in the oocyte include the exon junction
456 complex (EJC), which, together with the SOLE RNA structure, is essential for *osk* transport to
457 the posterior of the oocyte[46,76]. As Tm1 remains bound to the *osk* mRNP throughout transport
458 and is required for Khc-mediated translocation of the mRNA to the posterior of the oocyte[42,43],
459 it is likely that the activating factor(s) induces a conformational change in the Khc-Tm1 complex
460 rather than dissociation of Tm1. Investigating the molecular mechanisms that underpin these
461 dynamics is likely to inform our understanding of how kinesin-1 activity is orchestrated in other
462 transport systems.

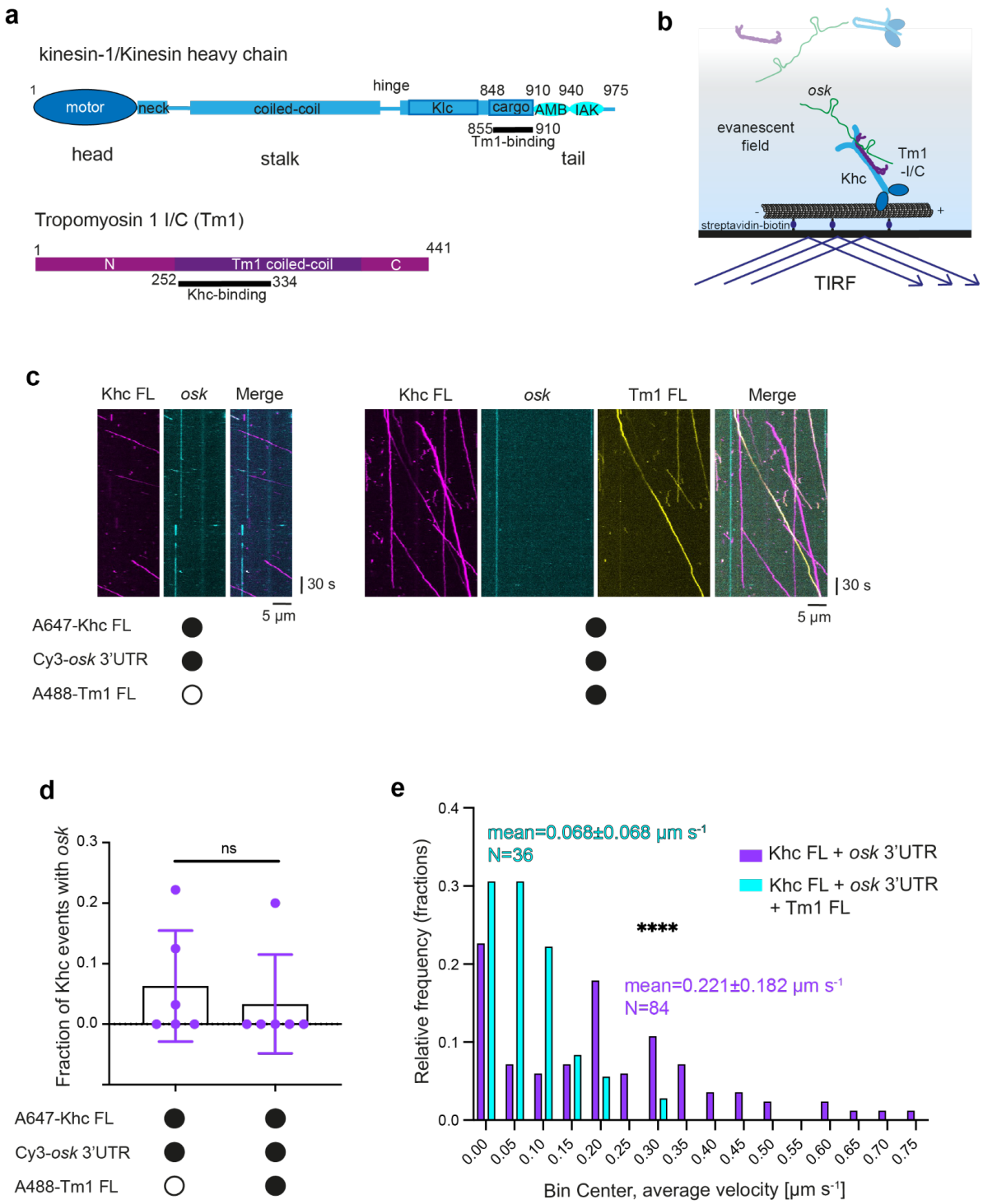

Figure 1: A TIRF microscopy-based *in vitro* motility assay reveals an inhibitory effect of Tm1 on Khc motility. a Scheme of domain architecture of *Drosophila* Kinesin heavy chain (Khc) and atypical Tropomyosin 1 isoform I/C (Tm1). **b** Scheme of *in vitro* motility assay. Preincubated Khc, Tm1 and RNA mixes were diluted to 6.25 nM of each component, and injected into an imaging chamber with pre-immobilised microtubules on a passivated glass surface. **c** Example kymographs showing processive movements of AlexaFluor647-labeled SNAP-Khc FL (labeling efficiency: 79.75 %), Cy3-labeled *osk* 3'UTR and AlexaFluor488-labeled Tm1 FL (labeling efficiency: 57 %). Microtubule plus and minus ends are oriented toward the right and left of each kymograph, respectively. **d** Fraction of Khc transporting *osk* 3'UTR in absence and presence of AlexaFluor488-labeled Tm1 in the assembly mix. Data points represent individual microtubules (84 and 36 complexes analyzed per condition). Statistical significance was evaluated with an unpaired t-test. ns = not significant. **e** Histograms of velocity distributions of Khc

475 in absence or presence of Tm1. Statistical significance was evaluated with an unpaired t-test.
476 ****$p<0.0001$.

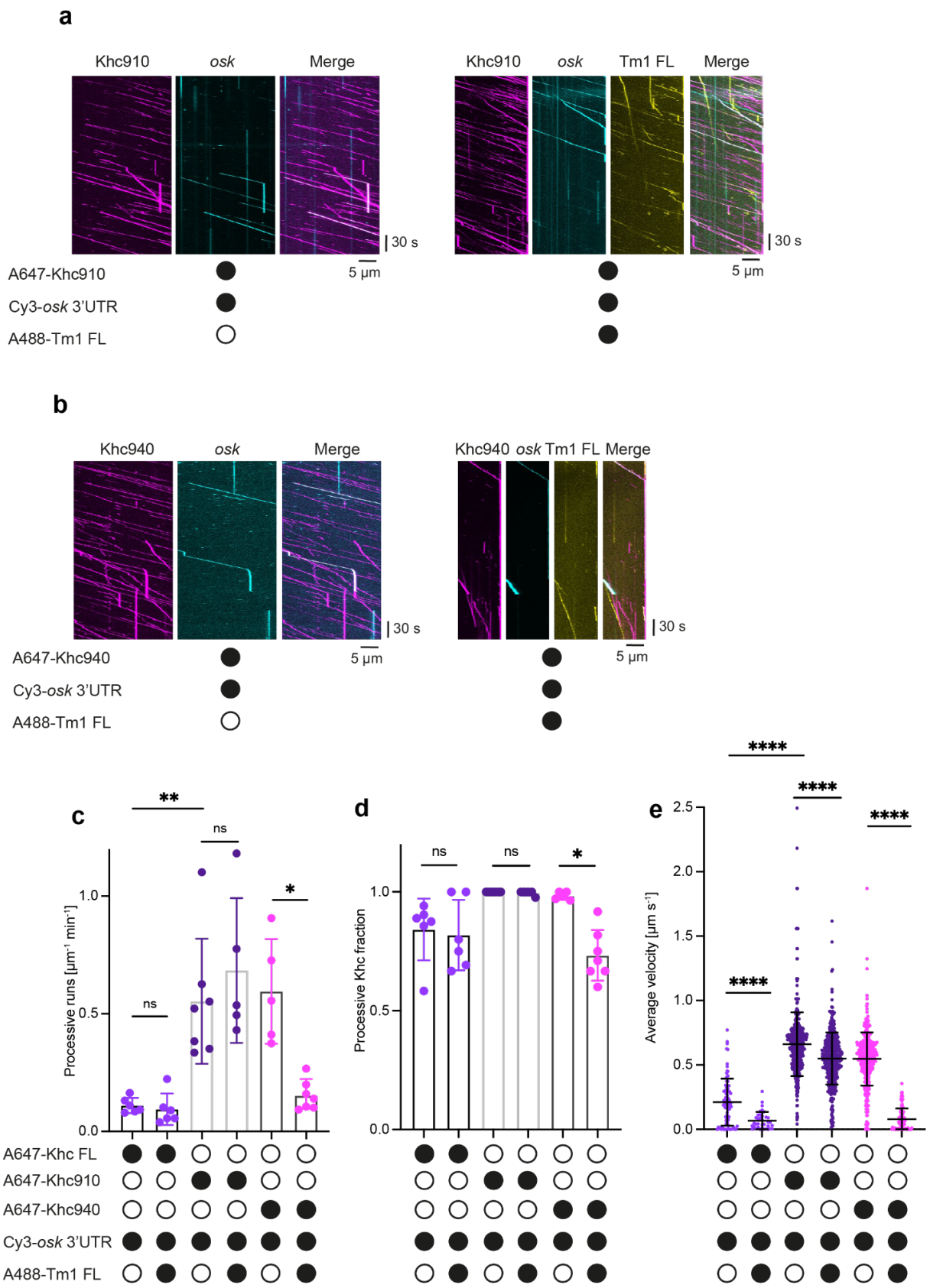

Figure 2: Tm1 inhibits Khc motility *in vitro* via Khc's regulatory tail. a, b Example kymographs showing processive movements of AlexaFluor647-labeled SNAP-Khc910 (a) and Khc940 (b) ± AlexaFluor488-labeled Tm1 FL. Microtubule plus and minus ends are oriented toward the right and left of each kymograph, respectively. **c, d** Number of processive events of Khc FL, Khc940 and Khc910 (c) and fraction of microtubule-bound Khc complexes that are processive ± Tm1 FL in the assembly mix

(d). Data points show values for individual microtubules (between 36 and 438 complexes analyzed per condition). Error bars: SD. Statistical significance was evaluated with an unpaired t-test. ns = not significant, **$p<0.01$, *$p<0.05$. Labeling efficiencies for Khc FL, Khc910 and Khc940 were 79.8 %, 54 % and 78 %, respectively, so that total run numbers are underestimated. **e** Average velocities of Khc FL and Khc910 ± Tm1 FL in the assembly mix. Data points represent individual runs. Statistical significance was evaluated with an unpaired t-test. ****$p<0.0001$.

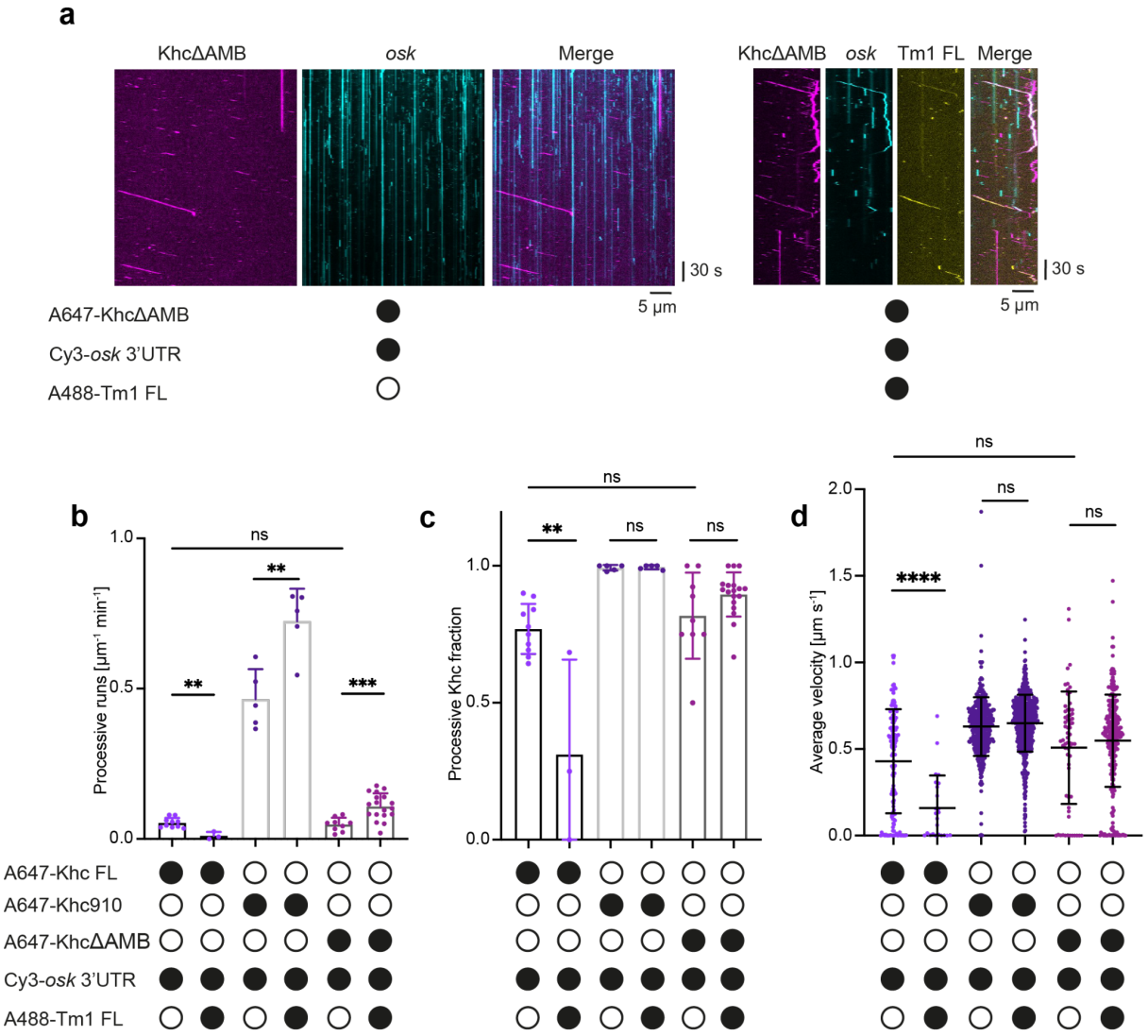

Figure 3: Khc AMB domain mediates Tm1 inhibition of Khc. a Example kymographs showing processive movements of AlexaFluor647-labeled SNAP-KhcΔAMB ± AlexaFluor488-labeled Tm1 FL in the assembly mix. Microtubule plus and minus ends are oriented toward the right and left of each kymograph, respectively. **b, c** Processive events of Khc FL, Khc910 and KhcΔAMB ± Tm1 FL (b) and fraction of processive Khc events (c). Data points show values for individual microtubules (between 24 and 595 complexes analyzed per condition). Error bars: SD. Statistical significance was evaluated with an unpaired t-test. ****p<0.0001, ***p<0.001, **p<0.01. Labeling efficiencies for Khc FL, Khc910 and KhcΔAMB were 79.8 %, 54 % and 78.8 %, respectively, so that total run numbers are underestimated. **d** Average velocities of Khc FL, Khc910 and KhcΔAMB ± Tm1 FL. Data points represent individual runs. Statistical significance was evaluated with an unpaired t-test. ****p<0.0001.

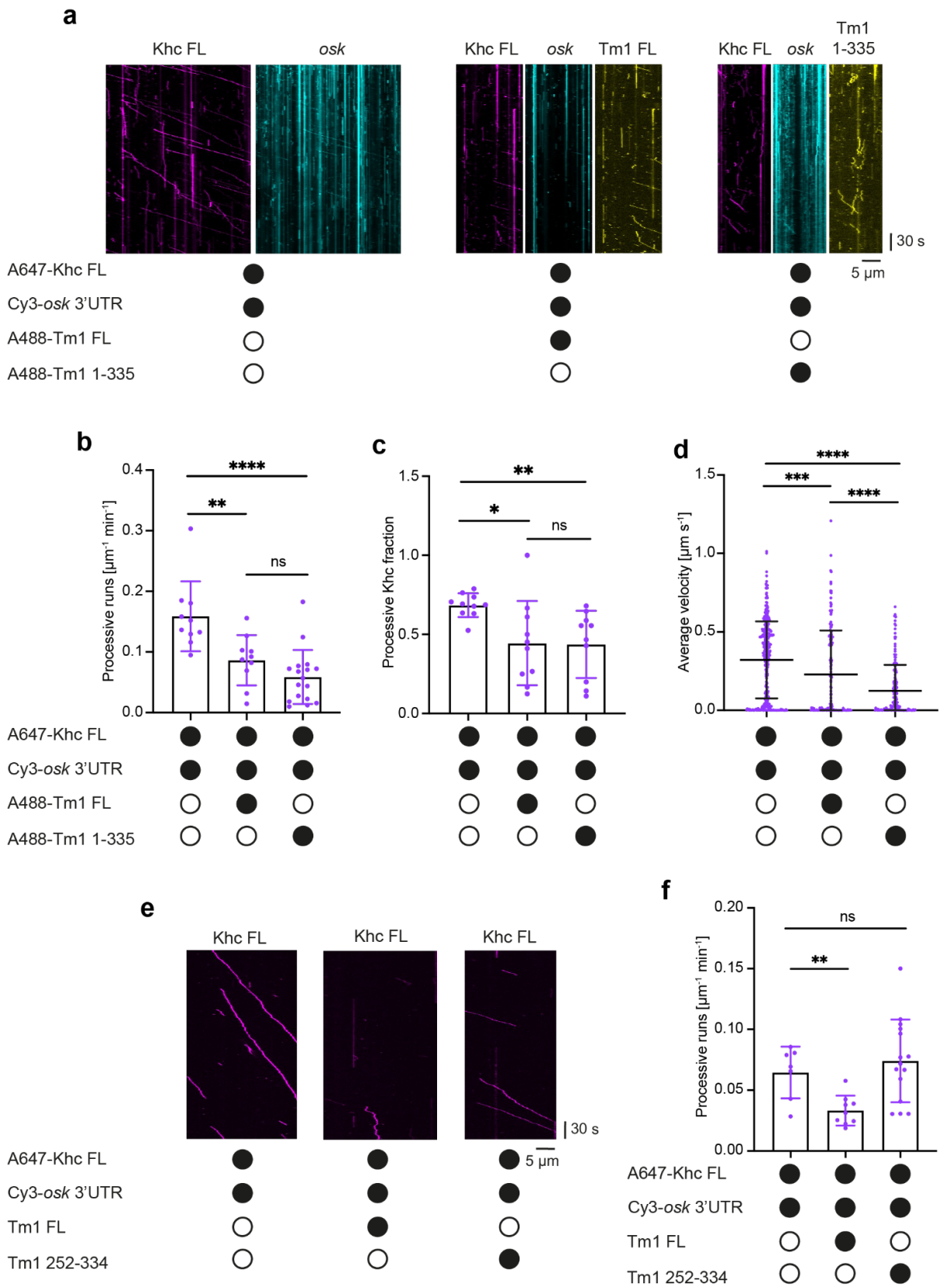

Figure 4: The Tm1 N-terminal region is required for Khc inhibition. a Example kymographs showing processive movements of AlexaFluor647-labeled SNAP-Khc FL ± AlexaFluor488-labeled Tm1 FL or Tm1 1-335 in the assembly mix. **b, c** Processive events of Khc FL ± Tm1 FL or Tm1 1-335 in the assembly mix (b) and fraction of processive Khc events (c). Data points show values for individual microtubules (between 44 and 335 complexes analyzed per condition). Error bars: SD. Statistical significance was evaluated with an unpaired t-test. ****p<0.0001, ***p<0.001. **d** Average velocities of Khc FL ± Tm1 FL or Tm1 1-335 in the assembly mix. Data points represent individual runs. Statistical

510 significance was evaluated with an unpaired t-test. ****p<0.0001. **e** Example kymographs showing
511 processive movements of AlexaFluor647-labeled SNAP-Khc FL ± Tm1 FL or Tm1 252-334. **f** Processive
512 events of Khc FL ± Tm1 FL or Tm1 252-334 in the assembly mix. Error bars: SD. Statistical significance
513 was evaluated with an unpaired t-test with Welch's correction. **p<0.01. Microtubule plus and minus
514 ends are oriented toward the right and left of each kymograph, respectively (a and e).

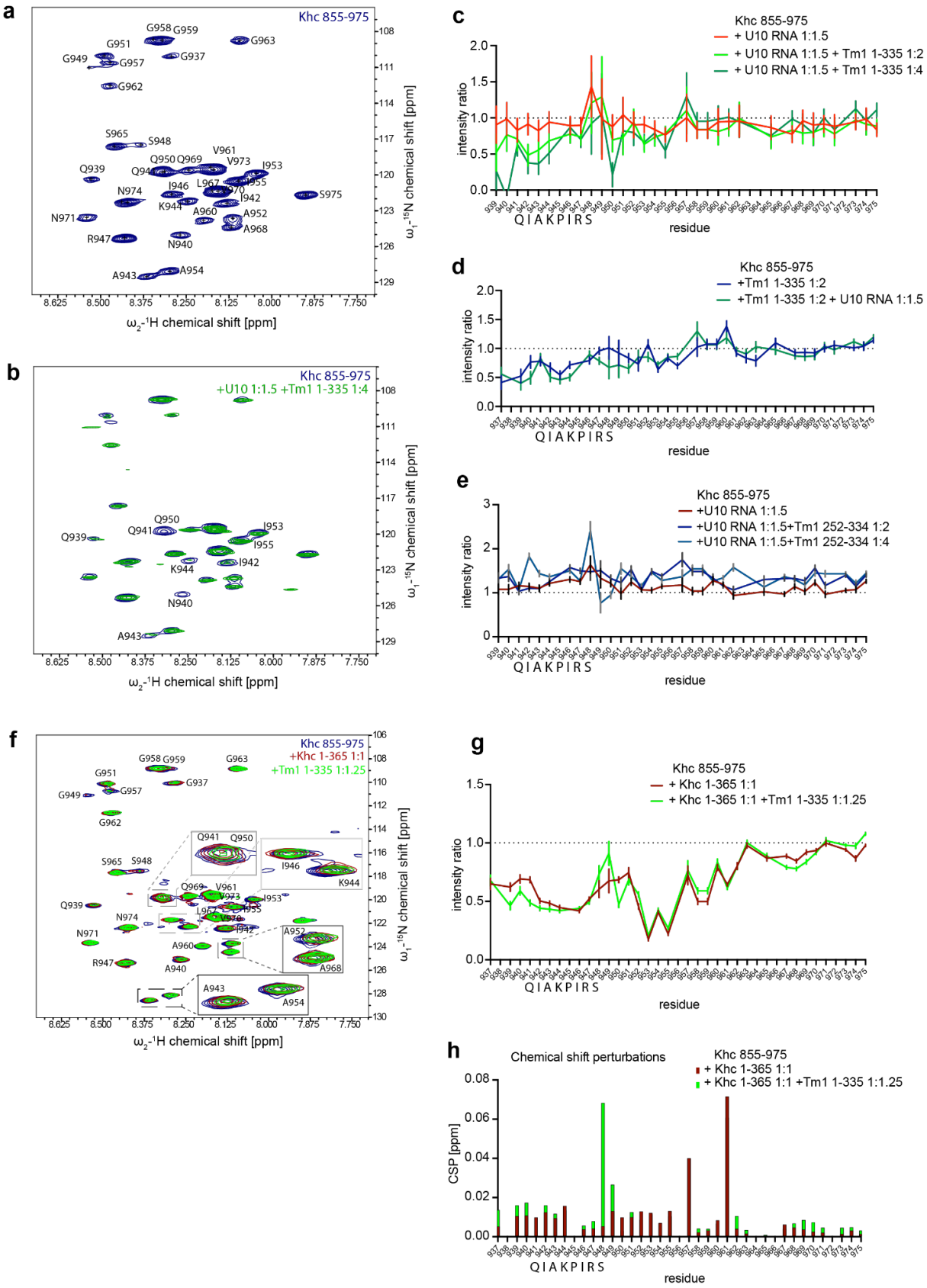

Figure 5: Tm1 binding affects the free and motor-bound regulatory tail of Khc. a ^{1}H,^{15}N-HSQC spectrum of the Khc tail construct Khc 855-975 with backbone assignments indicated. **b, c** ^{1}H,^{15}N-HSQC titration experiment with U10 RNA and Tm1 1-335. Overlaid spectra (b) and plotted intensity ratios of individual residues. RNA was added before Tm1. **d** Intensity ratios of a titration experiment with Tm1 1-335 and U10 RNA in which Tm1 was added before RNA. **e** Intensity ratios of a titration experiment with

522 U10 RNA and Tm1 252-334 in which RNA was added before Tm1. **f - h** $^{1}H,^{15}N$-HSQC titration
523 experiment of the Khc tail Khc 855-975 with the motor domain Khc 1-365 and Tm1 1-335. Overlaid
524 spectra (f), plotted intensity ratios (g) and chemical shift perturbation plot (h) of individual residues.
525 Khc 1-365 was added before Tm1 1-335.

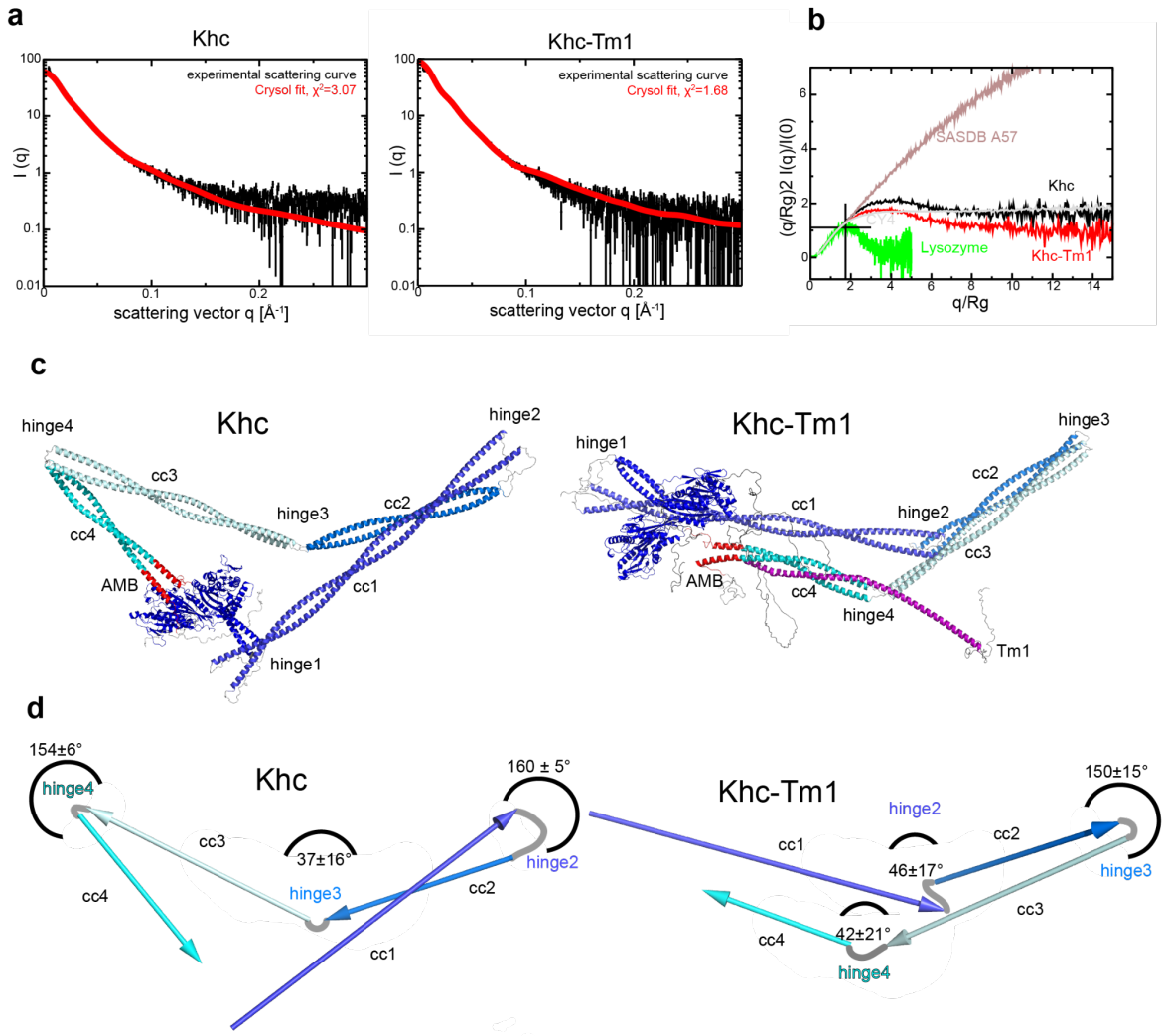

Figure 6: Khc conformation is altered upon Tm1 binding. a Experimental SAXS curves overlaid with theoretical SAXS curves of best Crysol fits. **b** Dimensionless Kratky plot of scattering profiles of Khc and the Khc-Tm1 complex compared to a globular protein (lysozyme), a disordered protein with short secondary structure elements (SASBDB[57] CY4) and a fully disordered extended protein (SASBDB[57] A57) to illustrate the differences between Khc and Khc-Tm1 and the contributions of ordered and disordered regions. **c** Best fits for Khc and for Khc-Tm1. Khc models are shown in shades of blue with the AMB domains marked in red, Tm1 is shown in pink. cc 1-4 denote the four coiled-coil regions of the Khc stalk domain. **d** Schemes showing the orientations of Khc's stalk coiled coils in the structures with best Crysol fits. Angles between coiled coils are averages from the five best-fitting models.

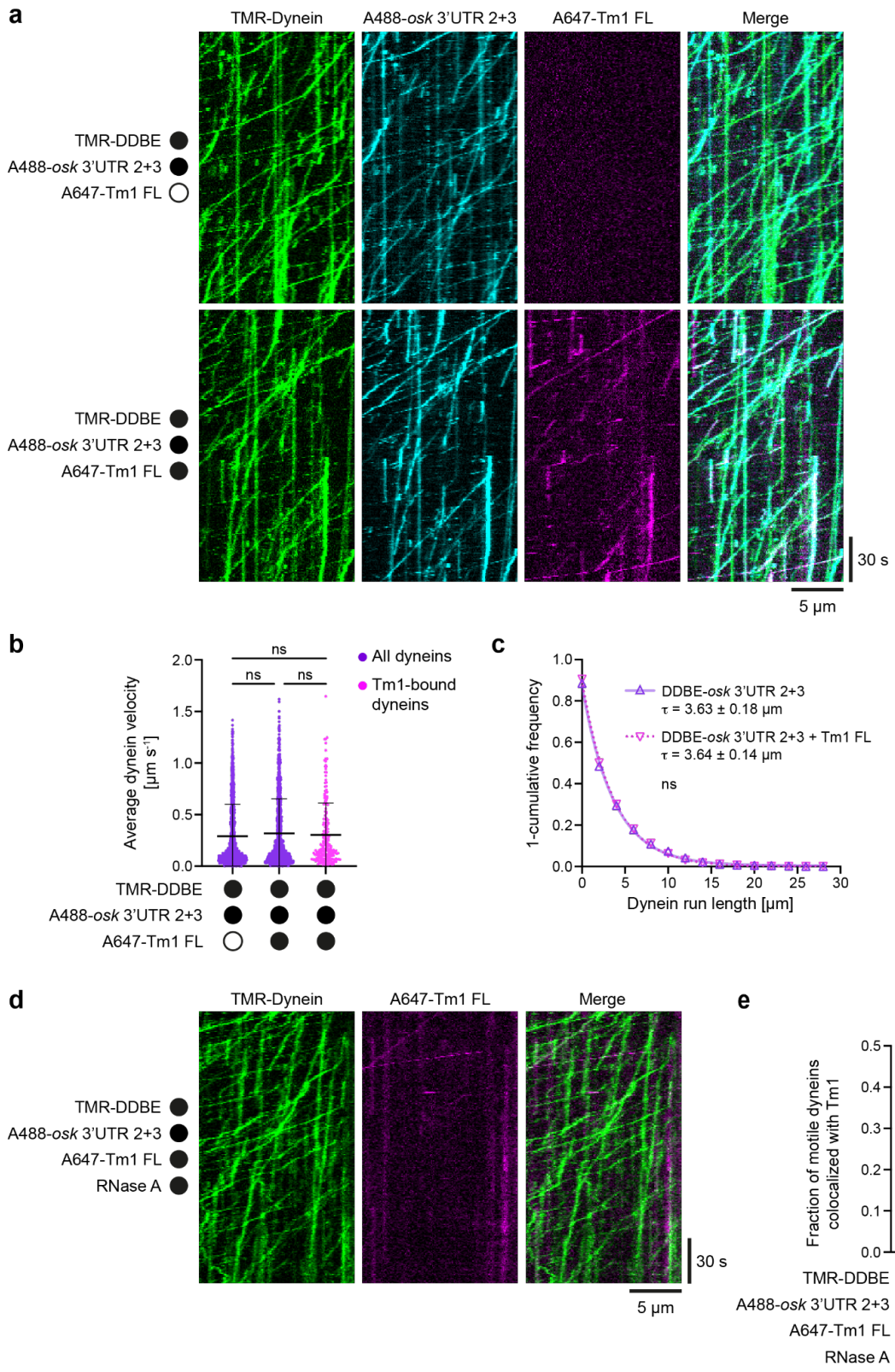

Figure 7: Tm1 does not affect dynein activity in *osk* RNPs. a Kymographs showing translocation of dynein and *osk* 3'UTR 2+3 in the presence and absence of Tm1 as part of minimal minus-end-directed RNPs containing dynein, dynactin, BicD, and Egalitarian (DDBE). Co-translocation of Tm1 is observed when present in the assay. **b, c** Average velocities (b) and run lengths (c) of DDBE-*osk* 3'UTR 2+3 complexes assembled with and without Tm1. 1-cumulative frequency distributions of measured run lengths were fit as one-phase decays with the decay constant τ ± 95 % confidence interval shown. Hollow triangles represent empirical bin values used for fitting. **d** Kymographs showing reduced association of Tm1 with motile DDBE-*osk* 3'UTR 2+3 RNPs after treatment with RNase A. **e** Fraction of moving DDBE-*osk* 3'UTR 2+3 RNPs that colocalized with Tm1 signal with and without RNase A

treatment. Dots represent values for individual complexes (b) or average values of all motility on individual microtubules (e). Microtubule plus and minus ends are oriented toward the right and left of each kymograph, respectively (a and d). For all plots, mean ± SD is shown. Statistical significance was determined by a Kruskal-Wallis ANOVA test (b), Mann-Whitney test (c), or Welch's t-test (e). ns: not significant. ****: $p<0.0001$.

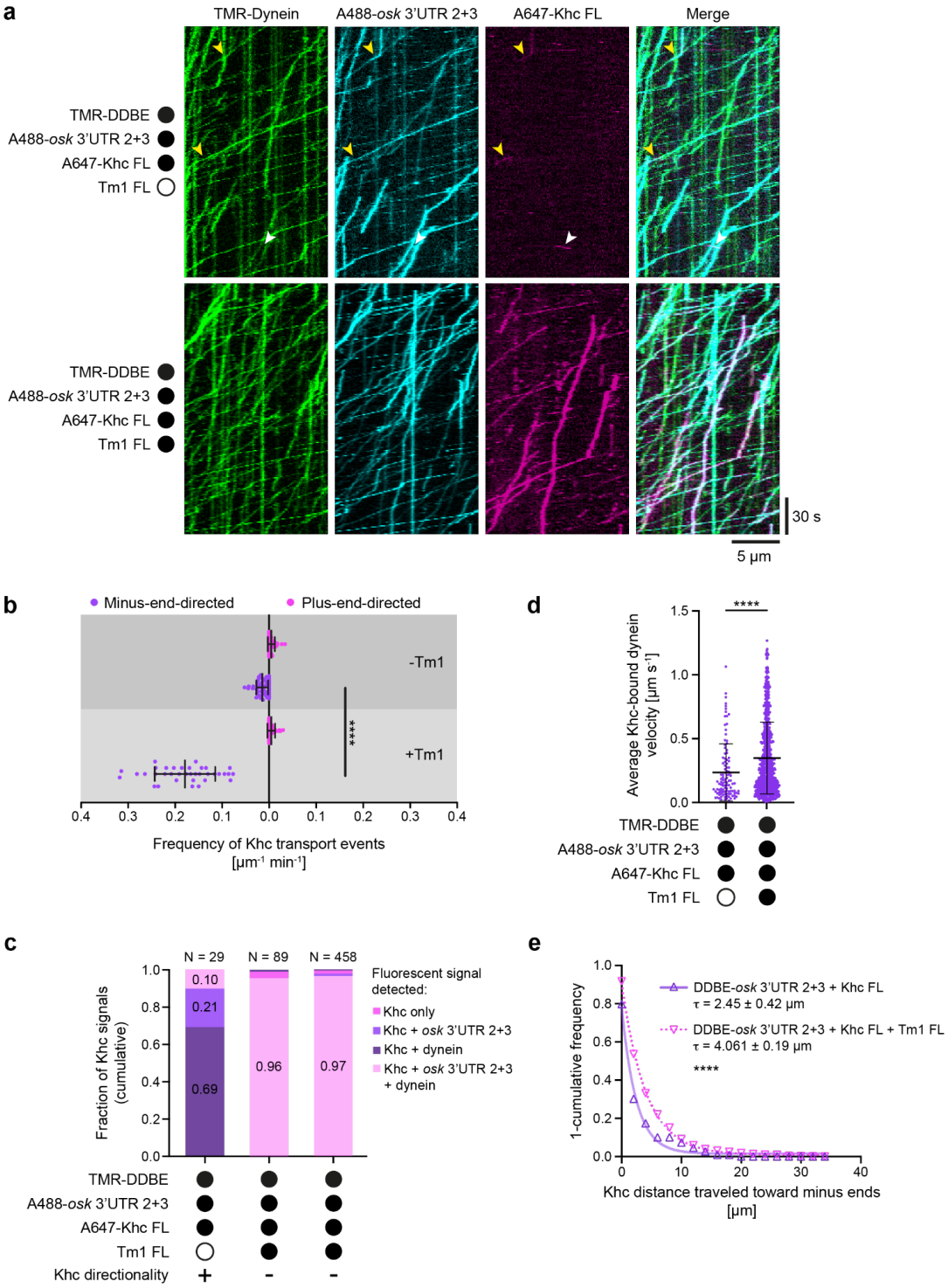

Figure 8: Tm1 promotes association of inhibited Khc with minus-end-directed DDBE-*osk* RNPs. **a** Kymographs showing motile behavior of DDBE (via TMR-dynein), AlexaFluor647-Khc, and AlexaFluor488 *osk* 3'UTR 2+3 in the presence and absence of unlabeled Tm1. Plus- and minus-end-directed Khc movements in the absence of Tm1 are indicated by white and yellow arrowheads, respectively. Microtubule plus and minus ends are oriented toward the right and left of each kymograph, respectively. **b** Frequency of processive Khc movements towards microtubule minus ends (towards left of x-axis, purple) and plus ends (towards right of x-axis, magenta) in the presence and absence of Tm1. **c** Cumulative fraction of plus- and minus-end-directed Khc signals that co-migrated with all combinations of other labeled assay components in the presence and absence of Tm1. **d** Average

velocities of minus-end-directed DDBE-*osk* 3'UTR 2+3 complexes with co-migrating Khc signal in the presence and absence of Tm1. **e** Distance traveled by Khc towards the minus end in the presence and absence of Tm1. 1-cumulative frequency distributions of measured run lengths were fit as one-phase decays with the decay constant $\tau \pm 95$ % confidence interval shown. Hollow triangles represent empirical bin values used for fitting. Dots represent average values for all motility on individual microtubules (b) or values for individual complexes (d). For all plots mean ± SD is shown. Statistical significance was determined by Welch's t-test (b) or Mann-Whitney test (d, e). ****: $p<0.0001$.

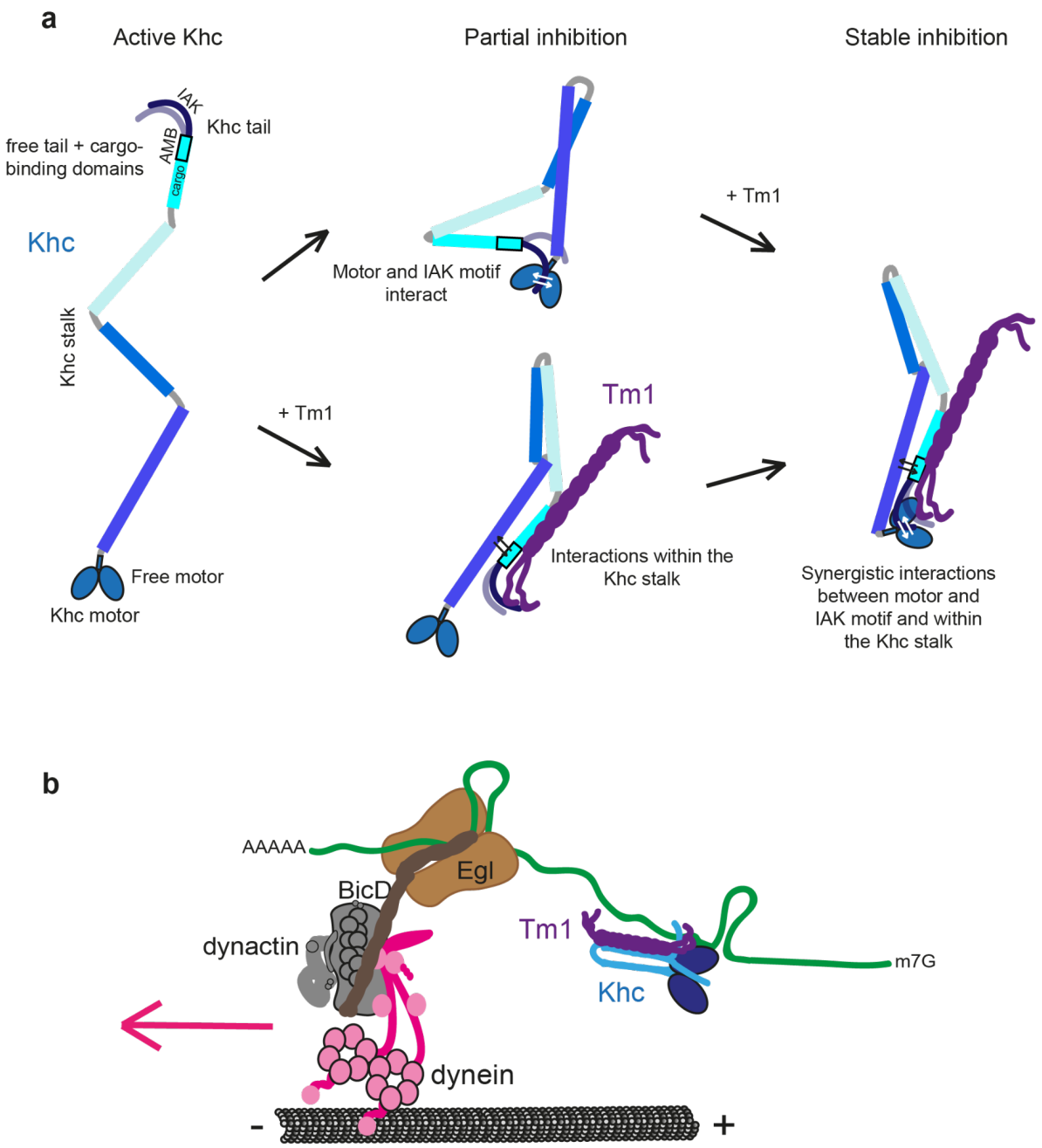

Figure 9: a Model of Tm1-mediated stabilization of the auto-inhibited conformation of Khc. Whereas both the motor domain-IAK peptide interaction and interactions within the Tm1-bound, rearranged Khc stalk region, including the AMB domain, can inhibit Khc partially, synergy between these weak interactions stabilizes the inhibiting head-tail interaction. **b** Model of Tm1's role in dynein-mediated transport of *osk*. By linking Khc to the dynein-transported *osk* RNA and keeping Khc inhibited, Tm1 allows the first, dynein-mediated transport step from the nurse cells to the oocyte to proceed without a tug-of-war between the motors. These events also position Khc on the RNP for the second, Khc-mediated transport step.

Materials and Methods

Molecular Cloning

Khc FL for *in vitro* studies was cloned with a HisSUMO-SNAP-3C-tag into MCS1 between BamHI and HindIII sites of the pFastBacDual vector by InFusion cloning (Takara). The Khc mutant constructs used for *in vitro* studies were generated by site-directed mutagenesis of the Khc FL plasmid using primers that either inserted a stop codon after aa 910 (Khc910) or aa 940 (Khc940) or deleted aa 911-938 (KhcΔAMB) followed by DpnI digest of the template plasmid and transformation of the product in *E. coli* XL1-blue cells. For co-expression of Khc FL and Tm1, the Tm1 coding sequence was inserted into MCS2 of pFastBacDual-HisSUMO-SNAP-3C-Khc between SmaI and KpnI sites by InFusion cloning (Takara). Tm1 FL for motility assays was cloned with a HisSUMO-SNAP-tag between SacI and HindIII sites of the pET11 vector by InFusion cloning (Takara). The SNAP-Tm1 1-335 truncation was made by site-directed mutagenesis of the SNAP-Tm1 FL plasmid using primers that inserted a stop codon after aa 335 as described above.

Protein expression and purification

His6-SUMO-SNAP-3C-tagged Khc FL, Khc910 or ΔIAK and ΔAMB truncations and co-expressed Khc-Tm1 complexes were expressed using the Bac-to-Bac Baculovirus expression system (Gibco). 1 L of *Sf21* insect cells at $1x10^6$ cells mL^{-1} shaking culture were infected with 10 mL of P1 virus stock. After expression for 3 d at 27.5 °C, cells were harvested by centrifugation at 1000 g for 20 min at 4°C. The pellets were lysed in a dounce tissue grinder in lysis buffer (20 mM Tris-HCl at pH 7.5, 500 mM NaCl, 1 mM $MgCl_2$, 0.1 mM ATP, 2 mM DTT, 5 % glycerol, 0.2 % Tween-20). The lysates were cleared by centrifugation and the soluble protein fraction was affinity-purified on a HisTrap Excel column (GE Healthcare). After elution in a 0–300 mM imidazole gradient, the HisSUMO-fusion tag was cleaved either by Senp2 (SNAP-tagged proteins for fluorescent labeling) or 3C protease (unlabeled proteins) digest during dialysis in GF150 buffer (25 mM HEPES/KOH pH 7.3, 150 mM KCl, 1 mM $MgCl_2$, 0.1 mM ATP, and 2 mM DTT) for 16 h before further purification by anion exchange chromatography on a HiTrap Q HP column (GE Healthcare), followed by size exclusion chromatography (SEC) on a Superdex 200 10/300 Increase column (GE Healthcare).

His6-SUMO-tagged and His6-SUMO-SNAP-tagged Tm1 protein constructs and GST-Khc 1-365 were expressed in BL21-CodonPlus(DE3)-RIL cells (Stratagene) by isopropyl β-D-1-thiogalactopyranoside (IPTG) induction for 16 h at 18 °C. Cells were grown in Luria-Bertani (LB) medium (0.5 % [w/v] yeast extract [MP], 1 % [w/v] tryptone [MP], 0.5 % [w/v] NaCl at pH 7.2) supplemented with antibiotics (100 µg mL^{-1} ampicillin or 10 µg mL^{-1} kanamycin and

616 34 µg mL^{-1} chloramphenicol). After harvesting, the pellets were lysed by a microfluidizer
617 processor (Microfluidics) in 20 mM Tris-HCl (pH 7.5), 500 mM NaCl, 5 % glycerol, 0.01 % NP-
618 40, and 40 mM imidazole buffer supplemented with protease inhibitor cocktail (Roche) and
619 2 mM DTT. The lysates were subsequently cleared by centrifugation. HisSUMO-tagged
620 proteins were affinity-purified by Ni-IMAC on a HisTrap column (Cytiva) and eluted with an
621 imidazole gradient (40–300 mM). After cleavage of the His6-SUMO-tag with Senp2 protease,
622 cleaved tags and protease were removed by a second, subtractive Ni-IMAC on a HisTrap
623 column (GE Healthcare). The proteins were further purified on either a 10/300 Superose 6
624 Increase GL or a HiLoad 16/600 Superdex 200 SEC column in either GF150 buffer for motility
625 assays or NMR buffer (25 mM $NaPO_4$ pH 6.5, 150 mM NaCl, and 0.5 mM TCEP) for NMR
626 experiments.
627
628 GST-tagged Khc 1-365 was affinity-purified on a GSTrap column (Cytiva) and glutathione
629 gradient (1-20 mM). The protein was further purified on a HiLoad 16/600 Superdex 200 SEC
630 column in GF150 buffer.
631
632 SNAP-tagged Khc and Tm1 proteins were fluorescently labeled with SNAP-Cell TMR Star,
633 SNAP-Surface Alexa Fluor 488 or SNAP-Surface Alexa Fluor 647 at 15 °C for 90 min in GF150
634 buffer with a 1.5x excess of dye. Free dye was removed by a subsequent desalting step on a
635 PD-10 desalting column (Cytiva). Labeling efficiencies were determined by measuring protein
636 concentration at 280 nm and dye concentration at the dye's excitation maximum. For
637 monomeric protein, labeling efficiency was calculated as $c_{dye}/c_{protein}$. For dimeric proteins,
638 labeling efficiency was calculated based on monomer labeling efficiencies as $(L_1 \times U_2) + (U_1 \times$
639 $L_2) + (L_1 \times L_2)$ with L1 = fraction of monomer 1 labeled, L2 = fraction of monomer 2 labeled, U1
640 = fraction of monomer 1 unlabeled, U2 = fraction of monomer 2 unlabeled.
641
642 Recombinant human dynein and *Drosophila* Egl-BicD complexes were expressed in *Sf9* insect
643 cells with the dynein complex fluorescently labeled via a SNAPf tag fused to the N-terminus of
644 Dynein heavy chain, as described previously[15]. Native porcine dynactin was purified from brain
645 tissue as described previously[15].

646 RNA *in vitro* transcription

647 The *osk* RNA constructs used for the motility assays were synthesized *in vitro* using the
648 MEGAscript T7 Transcription Kit (Ambion). The RNA was transcribed from a PCR product
649 amplified with a T7 promote-containing forward primer and containing an *osk* mRNA FL, *osk*
650 3'UTR or a ~529-nt region of the *osk* 3'UTR previously defined as region 2+3 (*osk* 3'UTR 2+3)
651 that is sufficient to promote the localization of reporter transcripts to the developing oocyte[48].
652 The template for *osk* min was generated from three overlapping primers by PCR and

653 subsequently amplified again with a T7 promoter containing forward primer. RNA was
654 transcribed from the final PCR product. For fluorescent labeling of the *osk* 3'UTR and *osk* min
655 transcripts, Cy3- or Cy5-UTP was included in the transcription reaction with a 4-fold excess of
656 unlabeled UTP, yielding transcripts with several labels per RNA molecule. For *osk* 3'UTR 2+3,
657 transcripts were fluorescently labeled with AlexaFluor488-UTP with a 5-fold excess of
658 unlabeled UTP. Transcripts were subsequently purified by phenol/chloroform extraction and
659 passed through a G50 mini Quick Spin RNA desalting column (Sigma-Aldrich) to remove
660 unincorporated nucleotides before sodium acetate/ethanol precipitation. The precipitated RNA
661 was resuspended in nuclease-free water and stored at -20 °C or -70 °C.

662 Polymerization and stabilization of microtubules

663 Microtubules were polymerized from porcine tubulin (Cytoskeleton Inc., Denver, CO) and
664 labeled with fluorophores and biotin by stochastic incorporation of labeled dimers into the
665 microtubule lattice. Mixes of 2.5 µM unlabelled tubulin, 0.17 µM Hilyte488- or AMCA-tubulin,
666 and 0.3 µM biotin-tubulin were incubated in BRB80 (80 mM PIPES pH 6.85, 2 mM $MgCl_2$,
667 0.5 mM EGTA, 1 mM DTT) with 0.67 mM GMPCPP (Jena Bioscience, Jena, Germany)
668 overnight at 37 °C. Polymerized microtubules were pelleted in a room temperature table top
669 centrifuge at 18,400 x g for 8.5 min, and washed once with pre-warmed (37 °C) BRB80. After
670 pelleting once more, the microtubules were gently resuspended in 300 µL pre-warmed (37 °C)
671 BRB80 containing 20-40 µM paclitaxel (taxol; Sigma-Aldrich).
672
673 Polarity marked microtubules with HiLyte 488 tubulin enriched at minus ends were made
674 according to the principle described previously[77]. Bright microtubule seeds were polymerized
675 at 37 ºC for 10 minutes in a mix containing 2.5 µM unlabelled porcine tubulin (5-fold excess
676 over fluorescent tubulin), 0.5 µM HiLyte 488 tubulin, and 0.3 µM biotin-tubulin in BRB80 with
677 0.67 mM GMPCPP. After 10 minutes, this mixture was diluted 1:1 with a tubulin polymerization
678 mix containing 12.5 µM unlabelled tubulin and 0.3 µM biotin-tubulin in BRB80 with 0.67 mM
679 GMPCPP for final tubulin concentrations of 7.5 µM unlabelled tubulin (30-fold excess over
680 fluorescent tubulin), 0.25 µM HiLyte 488 tubulin, and 0.3 µM biotin-tubulin. The final tubulin
681 mix was incubated at 37 ºC for an additional 2 h to allow growth of relatively dim microtubule
682 plus ends before harvesting and taxol stabilization as described above.

683 *In vitro* single-molecule reconstitution assays, TIRF microscopy and 684 image analysis

685 TIRF-based single-molecule reconstitution assays were performed as described previously[15].
686 Briefly, taxol-stabilized porcine microtubules were immobilized in imaging flow chambers by
687 streptavidin-based linkages to biotin-PEG passivated cover slips. Khc RNP assay mixes were

688 assembled at 500 nM of each component. Assemblies of the dynein transport machinery with
689 Khc and Tm1 contained 100 nM dynein, 200 nM dynactin, 500 nM Egl-BicD, 1 μM RNA,
690 500 nM Khc (or Khc storage buffer as a control) and 2 μM Tm1 (or Tm1 storage buffer as a
691 control), and were incubated on ice for 1-2 h prior to imaging. The RNP assay mixes were then
692 diluted to concentrations suitable for imaging of single molecules (6.25 nM for Khc RNP
693 experiments, 5 nM dynein and 25 nM Khc for experiments containing both motors) in BRB12
694 (Khc experiments) or modified dynein motility buffer[58] (30 mM HEPES-KOH pH 7.0, 50 mM
695 KCl, 5 mM $MgSO_4$, 1 mM EGTA pH 7.5, 1 mM DTT, 0.5 mg mL^{-1} BSA - experiments including
696 DDBE) supplemented with 1 mg mL^{-1} α-casein, 20 μM taxol, 2.5 mM MgATP and an oxygen
697 scavenging system (1.25 μM glucose oxidase, 140 nM catalase, 71 mM 2-mercaptoethanol,
698 25 mM glucose final concentrations) to reduce photobleaching, and applied to the flow
699 chamber for imaging by TIRF microscopy.
700
701 For assays in which RNase A was added, assemblies were diluted into modified dynein motility
702 buffer as described above with either 1 μL of 0.2 μg/mL RNase A (final concentration of
703 9.5 ng/mL) diluted in motility buffer, or 1 μL of motility buffer alone added in addition. Such low
704 concentrations of RNase A were used to ensure mild digestion of the RNA (which was
705 monitored during acquisition via the fluorescent RNA signal) that would eliminate any RNA-
706 based connections between protein components whilst limiting digestion of the predominantly
707 double-stranded localization signal important for activating DDBE motility[48]. These mixes were
708 incubated at room temperature for 5 min before application to the imaging chambers.
709
710 For each chamber, a single multi-color acquisition of 500 frames was made at a frame rate of
711 ~2 frames s^{-1} and 150 ms exposure (1-2 colors) or 1.2-1.4 frames s^{-1} and 50 ms exposure (3
712 colors). Images of Khc-Tm1 were acquired using a Leica GSD TIRF microscope system. All
713 images involving the dynein machinery were acquired on a Nikon TIRF system using
714 Micromanager control software[78] as described previously[15].
715
716 Binding and motility of RNP components in the *in vitro* reconstitution assays were manually
717 analyzed by kymograph in FIJI[79] as described previously[15]. Statistical analysis and plotting
718 were performed using GraphPad Prism version 9.1.1 for MacOS, (GraphPad Software, San
719 Diego, USA).
720 As we noticed some variability of Khc activities between different assays, we repeated all
721 appropriate control conditions for each experiment on the same day and used these
722 controls as comparison for our analysis. Results were confirmed on multiple days in
723 duplicates or triplicates of the experiments.

724 ## Microtubule binding assays

725 For microtubule binding assays, microtubules were polymerized from 5 mg mL^{-1} porcine tubulin
726 (Cytoskeleton Inc., Denver, CO) at 37 °C for 20 min in BRB80 supplemented with 1 mM GTP
727 and then diluted 1:10 in BRB80 + 20 µM taxol. Proteins of interest were incubated at indicated
728 concentrations with 20 µL of this microtubule solution for 30 min at RT in a final volume of
729 50 µL, before soluble and microtubule-bound fractions were segregated by ultracentrifugation
730 at 80,000 g for 30 min over a 500 µL 30 % sucrose cushion. Soluble fractions were
731 supplemented with 1x SDS-loading dye. Microtubule pellets were washed with BRB80 + taxol
732 before redissolving in 50 µL 1x SDS-loading dye. Soluble and pellet fractions were analyzed
733 by SDS-PAGE.

734 ## GST-pulldown competition assay

735 To test whether Tm1 competes with the Khc motor-tail interaction, 5 µM GST-Khc 855-975 as
736 bait and an indicated excess of prey protein Khc 1-365 were incubated with increasing
737 concentrations of Tm1 1-335 as competitor for Khc 855-975 binding in a total volume of 100 µL
738 in GF150 buffer (25 mM HEPES/KOH pH 7.3, 150 mM KCl, 1 mM $MgCl_2$, 2 mM DTT). After
739 incubation for 40 min on ice, the mixture was added to pre-equilibrated 50 µL Glutathione
740 Sepharose 4B beads (GE Healthcare) and proteins were allowed to bind for 2 h at 4 °C on a
741 nutating shaker. Beads were washed with 4 x 500 µL and 1 x 100 µL GF150 + 0.01 % NP-40.
742 Bound proteins were eluted from the beads by boiling in 1x SDS-loading dye for 5 min at 95 °C.
743 Input, wash and elution samples were analyzed by SDS-PAGE.

744 ## Mass photometry

745 Mass photometry data were acquired on a ReFeyn OneMP from co-expressed, co-purified
746 Khc-Tm1 complexes at a sample concentration of 20 nM in PBS. Data acquisition was
747 performed using AcquireMP, with data analysis performed in DiscoverMP (Refeyn Ltd, v1.2.3).

748 ## NMR spectroscopy

749 NMR measurements were performed at 298 K on a Bruker Avance III NMR spectrometer with
750 magnetic field strengths corresponding to proton Larmor frequencies of 600 MHz equipped
751 with a cryogenic triple resonance gradient probe head. NMR sample concentration was 50 µM
752 for titration experiments and 177 µM for backbone assignment experiments. Experiments for
753 backbone assignments were performed on ^{13}C,^{15}N-labeled samples using conventional triple-
754 resonance experiments (HNCO, HNCA, CBCA(CO)NH, HN(CO)CA and HNCACB)[80]. All
755 spectra were acquired using the apodization weighted sampling scheme[81] and processed
756 using NMRPipe[82]. Resonance assignments were done with the program Cara.
757

758 For titrations, RNA and Tm1 were added to ^{15}N-labeled Khc 855-975 at indicated ratios and a
759 ^{1}H,^{15}N-HSQC was recorded for each titration point. Peak intensity ratios were derived using
760 NMRView[83] and corrected for dilution. The extent of amide ^{1}H-^{15}N chemical shift perturbations
761 (CSPs) in free versus bound Khc 855-975 were calculated according to Williamson[84] to
762 compensate for frequency range differences between ^{15}N and ^{1}H dimensions.

763 SAXS data acquisition and structure modeling

764 SAXS data on full length Khc in isolation and in complex with full length Tm1 in 25 mM
765 HEPES/KOH pH 7.3, 150 mM KCl, 1 mM $MgCl_2$ and 2 mM DTT at concentrations of 0.5, 1.0
766 and 2.0 mg mL^{-1} were recorded at 20 °C on BM29 beamline, ESRF Grenoble, France. Ten
767 frames with an exposure time of 1 s/frame were recorded in batch mode using an X-ray
768 wavelength of 0.992 Å and a sample distance of 2.81 m to the Pilatus2M detector. Data
769 reduction and buffer subtraction was performed by the automatic processing pipeline[85]. R_g and
770 *I(0)* were determined using the Guinier approximation using Primus/autorg[86].
771
772 The scattering curve was subsequently compared to pools of structures generated by
773 connecting AlphaFold2[55,56] models of the Khc head domain (residues 1-378) homodimer
774 connected to four stretches of coiled-coil homodimers (residues 403-585, 604-706, 711-838
775 and 844-936 respectively). The linker regions between the structured parts were modified by
776 random phi/psi rotations in monomer A of the homodimer followed by a short four-step
777 simulated annealing energy minimization to restore proper bond geometries in monomer B,
778 for which all corresponding residues were rotated together with monomer A during the linker
779 randomization. The C-termini of monomer A and monomer B were subsequently randomized
780 independently. A total of 5000 structures were generated in this way. In a second step, the
781 structure of the motor homodimer was replaced by a homodimer (residues 1-344) bound to a
782 peptide from the C-terminus of molecule A (residues 934-953) containing the IAK motif, which
783 was followed by simulated annealing energy minimization to restore proper bond geometry.
784 During the simulated annealing energy minimization steps, the structures of the motor and
785 coiled-coil models or motor/peptide were unaltered by using a harmonic energy term to keep
786 the coordinates close to the starting coordinates in the template structure[87]. The calculations
787 were performed using CNS1.2[88] within the ARIA1.2 framework[89]. Structure pools for the Khc
788 homodimer in complex with Tm1 were generated in a similar way with an AlphaFold2-modeled
789 α-helix of Tm1 (residues 258-386) bound to the last coiled-coil stretch of Khc (residues 844-
790 936) in a position derived from the X-ray structure of the Khc-Tm1 complex[43] and additional
791 randomization of all residues outside the α-helix of Tm1. Each of the 2x5000 models were
792 fitted to the SAXS scattering intensities using CRYSOL[86].

Competing interest statement

The authors declare no competing interests.

Acknowledgements

We thank Lyudmila Dimitrova-Paternoga for reagents, the EMBL Protein Expression and Purification Core Facility, especially Karine Lapouge, the EMBL Advanced Light Microscopy Facility, especially Marko Lampe, and the EMBL Chemical Biology Core Facility, especially David Will, for their support. We thank the Bio-SAXS beamline at European Synchrotron Radiation Facility Grenoble, BM29. We thank Petra Pernot (ESRF), Jérôme Kieffer (ESRF) and Cy Jeffries (EMBL Hamburg) for discussions. S.H. was supported by the EMBL Interdisciplinary Postdoctoral fellowship (EIPOD) Programme under Marie Curie Cofund Actions MSCA-COFUND-FP (664726) and Deutsche Forschungsgemeinschaft (DFG)-Forschergruppe 2333 grant (EP37/4-1) to A.E.. Work in the laboratories of J.H. and A.E. was supported by funding from the DFG via the priority program SPP1935 to J.H. and A.E. (EP37/3-1 and EP37/3-2) and the EMBL. Work in S.L.B.'s group is supported by the Medical Research Council (MRC), as part of United Kingdom Research and Innovation (also known as UK Research and Innovation) [MRC file reference number MC_U105178790]. M.A.M. is supported by a project grant from the BBSRC (BB/T00696X/1). For the purpose of the MRC open access policy, the authors have applied a CC-BY public copyright license to any Author Accepted Manuscript version arising.

Author contributions

S.H., M.A.M., A.E., and S.L.B. conceived the study. S.H., M.A.M. and B.S. performed the experiments. S.H., M.A.M., B.S. and J.H. analyzed the data. S.L.B. and A.E. supervised the study. S.H. drafted the manuscript. All authors contributed to the writing of the manuscript.

References

1. Titus, M. A. Myosin-Driven Intracellular Transport. *Cold Spring Harb. Perspect. Biol.* **10**, (2018).
2. Doyle, M. & Kiebler, M. A. Mechanisms of dendritic mRNA transport and its role in synaptic tagging. *EMBO J.* **30**, 3540–3552 (2011).
3. Rodrigues, E. C., Grawenhoff, J., Baumann, S. J., Lorenzon, N. & Maurer, S. P. Mammalian Neuronal mRNA Transport Complexes: The Few Knowns and the Many Unknowns. *Front. Integr. Neurosci.* **15**, 692948 (2021).
4. Misgeld, T. & Schwarz, T. L. Mitostasis in neurons: maintaining mitochondria in an extended cellular architecture. *Neuron* **96**, 651–666 (2017).
5. Welte, M. A. Bidirectional transport along microtubules. *Curr. Biol.* **14**, R525-37 (2004).
6. Hancock, W. O. Bidirectional cargo transport: moving beyond tug of war. *Nat. Rev. Mol. Cell Biol.* **15**, 615–628 (2014).
7. McKenney, R. J., Huynh, W., Tanenbaum, M. E., Bhabha, G. & Vale, R. D. Activation of cytoplasmic dynein motility by dynactin-cargo adapter complexes. *Science* **345**, 337–341 (2014).
8. Schlager, M. A., Hoang, H. T., Urnavicius, L., Bullock, S. L. & Carter, A. P. In vitro reconstitution of a highly processive recombinant human dynein complex. *EMBO J.* **33**, 1855–1868 (2014).
9. Zhang, K. *et al.* Cryo-EM Reveals How Human Cytoplasmic Dynein Is Auto-inhibited and Activated. *Cell* **169**, 1303-1314.e18 (2017).
10. Reck-Peterson, S. L., Redwine, W. B., Vale, R. D. & Carter, A. P. The cytoplasmic dynein transport machinery and its many cargoes. *Nat. Rev. Mol. Cell Biol.* **19**, 382–398 (2018).
11. Olenick, M. A. & Holzbaur, E. L. F. Dynein activators and adaptors at a glance. *J. Cell Sci.* **132**, (2019).
12. Dienstbier, M., Boehl, F., Li, X. & Bullock, S. L. Egalitarian is a selective RNA-binding protein linking mRNA localization signals to the dynein motor. *Genes Dev.* **23**, 1546–1558 (2009).
13. Bullock, S. L. & Ish-Horowicz, D. Conserved signals and machinery for RNA transport in Drosophila oogenesis and embryogenesis. *Nature* **414**, 611–616 (2001).
14. Sladewski, T. E. *et al.* Recruitment of two dyneins to an mRNA-dependent Bicaudal D transport complex. *eLife* **7**, (2018).
15. McClintock, M. A. *et al.* RNA-directed activation of cytoplasmic dynein-1 in reconstituted transport RNPs. *eLife* **7**, (2018).
16. Lawrence, C. J. *et al.* A standardized kinesin nomenclature. *J. Cell Biol.* **167**, 19–22 (2004).
17. Stock, M. F. *et al.* Formation of the compact confomer of kinesin requires a COOH-terminal heavy chain domain and inhibits microtubule-stimulated ATPase activity. *J. Biol. Chem.* **274**, 14617–14623 (1999).
18. Kaan, H. Y. K., Hackney, D. D. & Kozielski, F. The structure of the kinesin-1 motor-tail complex reveals the mechanism of autoinhibition. *Science* **333**, 883–885 (2011).
19. Hackney, D. D. & Stock, M. F. Kinesin's IAK tail domain inhibits initial microtubule-stimulated ADP release. *Nat. Cell Biol.* **2**, 257–260 (2000).
20. Verhey, K. J. & Hammond, J. W. Traffic control: regulation of kinesin motors. *Nat. Rev. Mol. Cell Biol.* **10**, 765–777 (2009).
21. Cai, D., Hoppe, A. D., Swanson, J. A. & Verhey, K. J. Kinesin-1 structural organization and conformational changes revealed by FRET stoichiometry in live cells. *J. Cell Biol.* **176**, 51–63 (2007).
22. Chiba, K., Ori-McKenney, K. M., Niwa, S. & McKenney, R. J. Synergistic autoinhibition and activation mechanisms control kinesin-1 motor activity. *Cell Rep.* **39**, 110900 (2022).
23. Diefenbach, R. J., Mackay, J. P., Armati, P. J. & Cunningham, A. L. The C-terminal region of the stalk domain of ubiquitous human kinesin heavy chain contains the binding site for kinesin light chain. *Biochemistry* **37**, 16663–16670 (1998).
24. Verhey, K. J. *et al.* Light chain-dependent regulation of Kinesin's interaction with microtubules. *J. Cell Biol.* **143**, 1053–1066 (1998).
25. Pernigo, S., Lamprecht, A., Steiner, R. A. & Dodding, M. P. Structural basis for kinesin-1:cargo

871 recognition. *Science* **340**, 356–359 (2013).
872 26. Fenton, A. R., Jongens, T. A. & Holzbaur, E. L. F. Mitochondrial adaptor TRAK2 activates and
873 functionally links opposing kinesin and dynein motors. *Nat. Commun.* **12**, 4578 (2021).
874 27. Canty, J. T., Hensley, A. & Yildiz, A. Mitochondrial TRAK adaptors coordinate dynein and
875 kinesin motility. *BioRxiv* (2021) doi:10.1101/2021.07.30.454553.
876 28. Arimoto, M. *et al.* The Caenorhabditis elegans JIP3 protein UNC-16 functions as an adaptor to
877 link kinesin-1 with cytoplasmic dynein. *J. Neurosci.* **31**, 2216–2224 (2011).
878 29. Celestino, R. *et al.* JIP3 interacts with dynein and kinesin-1 to regulate bidirectional organelle
879 transport. *J. Cell Biol.* **221**, (2022).
880 30. Kendrick, A. A. *et al.* Hook3 is a scaffold for the opposite-polarity microtubule-based motors
881 cytoplasmic dynein-1 and KIF1C. *J. Cell Biol.* **218**, 2982–3001 (2019).
882 31. Siddiqui, N. *et al.* PTPN21 and Hook3 relieve KIF1C autoinhibition and activate intracellular
883 transport. *Nat. Commun.* **10**, 2693 (2019).
884 32. Ephrussi, A. & Lehmann, R. Induction of germ cell formation by oskar. *Nature* **358**, 387–392
885 (1992).
886 33. Clark, A., Meignin, C. & Davis, I. A Dynein-dependent shortcut rapidly delivers axis
887 determination transcripts into the Drosophila oocyte. *Development* **134**, 1955–1965 (2007).
888 34. Zimyanin, V. L. *et al.* In vivo imaging of oskar mRNA transport reveals the mechanism of
889 posterior localization. *Cell* **134**, 843–853 (2008).
890 35. Brendza, R. P., Serbus, L. R., Duffy, J. B. & Saxton, W. M. A function for kinesin I in the
891 posterior transport of oskar mRNA and Staufen protein. *Science* **289**, 2120–2122 (2000).
892 36. Roth, S. & Lynch, J. A. Symmetry breaking during Drosophila oogenesis. *Cold Spring Harb.*
893 *Perspect. Biol.* **1**, a001891 (2009).
894 37. Navarro, C., Puthalakath, H., Adams, J. M., Strasser, A. & Lehmann, R. Egalitarian binds
895 dynein light chain to establish oocyte polarity and maintain oocyte fate. *Nat. Cell Biol.* **6**, 427–
896 435 (2004).
897 38. Trcek, T. & Lehmann, R. Germ granules in Drosophila. *Traffic* **20**, 650–660 (2019).
898 39. Loiseau, P., Davies, T., Williams, L. S., Mishima, M. & Palacios, I. M. Drosophila PAT1 is
899 required for Kinesin-1 to transport cargo and to maximize its motility. *Development* **137**, 2763–
900 2772 (2010).
901 40. Palacios, I. M. & St Johnston, D. Kinesin light chain-independent function of the Kinesin heavy
902 chain in cytoplasmic streaming and posterior localisation in the Drosophila oocyte.
903 *Development* **129**, 5473–5485 (2002).
904 41. Veeranan-Karmegam, R., Boggupalli, D. P., Liu, G. & Gonsalvez, G. B. A new isoform of
905 Drosophila non-muscle Tropomyosin 1 interacts with Kinesin-1 and functions in oskar mRNA
906 localization. *J. Cell Sci.* **129**, 4252–4264 (2016).
907 42. Gáspár, I., Sysoev, V., Komissarov, A. & Ephrussi, A. An RNA-binding atypical tropomyosin
908 recruits kinesin-1 dynamically to oskar mRNPs. *EMBO J.* **36**, 319–333 (2017).
909 43. Dimitrova-Paternoga, L. *et al.* Molecular basis of mRNA transport by a kinesin-1-atypical
910 tropomyosin complex. *Genes Dev.* **35**, 976–991 (2021).
911 44. Gáspár, I. *et al.* An RNA-based feed-forward mechanism ensures motor switching in oskar
912 mRNA transport. *BioRxiv* (2021) doi:10.1101/2021.04.24.441269.
913 45. Sanghavi, P., Laxani, S., Li, X., Bullock, S. L. & Gonsalvez, G. B. Dynein associates with oskar
914 mRNPs and is required for their efficient net plus-end localization in Drosophila oocytes. *PLoS*
915 *ONE* **8**, e80605 (2013).
916 46. Ghosh, S., Marchand, V., Gáspár, I. & Ephrussi, A. Control of RNP motility and localization by
917 a splicing-dependent structure in oskar mRNA. *Nat. Struct. Mol. Biol.* **19**, 441–449 (2012).
918 47. Simon, B., Masiewicz, P., Ephrussi, A. & Carlomagno, T. The structure of the SOLE element of
919 oskar mRNA. *RNA* **21**, 1444–1453 (2015).
920 48. Jambor, H., Mueller, S., Bullock, S. L. & Ephrussi, A. A stem-loop structure directs oskar
921 mRNA to microtubule minus ends. *RNA* **20**, 429–439 (2014).
922 49. Seeger, M. A. & Rice, S. E. Microtubule-associated protein-like binding of the kinesin-1 tail to
923 microtubules. *J. Biol. Chem.* **285**, 8155–8162 (2010).
924 50. Navone, F. *et al.* Cloning and expression of a human kinesin heavy chain gene: interaction of
925 the COOH-terminal domain with cytoplasmic microtubules in transfected CV-1 cells. *J. Cell*

Biol. **117**, 1263–1275 (1992).
51. Jolly, A. L. *et al.* Kinesin-1 heavy chain mediates microtubule sliding to drive changes in cell shape. *Proc Natl Acad Sci USA* **107**, 12151–12156 (2010).
52. Goode, B. L. & Feinstein, S. C. Identification of a novel microtubule binding and assembly domain in the developmentally regulated inter-repeat region of tau. *J. Cell Biol.* **124**, 769–782 (1994).
53. Kikhney, A. G. & Svergun, D. I. A practical guide to small angle X-ray scattering (SAXS) of flexible and intrinsically disordered proteins. *FEBS Lett.* **589**, 2570–2577 (2015).
54. Receveur-Brechot, V. & Durand, D. How random are intrinsically disordered proteins? A small angle scattering perspective. *Curr. Protein Pept. Sci.* **13**, 55–75 (2012).
55. Jumper, J. *et al.* Highly accurate protein structure prediction with AlphaFold. *Nature* **596**, 583–589 (2021).
56. Evans, R. *et al.* Protein complex prediction with AlphaFold-Multimer. *BioRxiv* (2021) doi:10.1101/2021.10.04.463034.
57. Kikhney, A. G., Borges, C. R., Molodenskiy, D. S., Jeffries, C. M. & Svergun, D. I. SASBDB: Towards an automatically curated and validated repository for biological scattering data. *Protein Sci.* **29**, 66–75 (2020).
58. Fumagalli, L. *et al.* C9orf72-derived arginine-containing dipeptide repeats associate with axonal transport machinery and impede microtubule-based motility. *Sci. Adv.* **7**, (2021).
59. Hisanaga, S. *et al.* The molecular structure of adrenal medulla kinesin. *Cell Motil. Cytoskeleton* **12**, 264–272 (1989).
60. Friedman, D. S. & Vale, R. D. Single-molecule analysis of kinesin motility reveals regulation by the cargo-binding tail domain. *Nat. Cell Biol.* **1**, 293–297 (1999).
61. Weijman, J. F. *et al.* Molecular architecture of the autoinhibited kinesin-1 lambda particle. *Sci. Adv.* **8**, (2022).
62. Williams, L. S., Ganguly, S., Loiseau, P., Ng, B. F. & Palacios, I. M. The auto-inhibitory domain and ATP-independent microtubule-binding region of Kinesin heavy chain are major functional domains for transport in the Drosophila germline. *Development* **141**, 176–186 (2014).
63. Tan, Z. *et al.* Autoinhibited kinesin-1 adopts a hierarchical folding pattern. *BioRxiv* (2023) doi:10.1101/2023.01.26.525761.
64. Cassella, L. & Ephrussi, A. Subcellular spatial transcriptomics identifies three mechanistically different classes of localizing RNAs. *Nat. Commun.* **13**, 6355 (2022).
65. Gardiol, A. & St Johnston, D. Staufen targets coracle mRNA to Drosophila neuromuscular junctions and regulates GluRIIA synaptic accumulation and bouton number. *Dev. Biol.* **392**, 153–167 (2014).
66. Derr, N. D. *et al.* Tug-of-war in motor protein ensembles revealed with a programmable DNA origami scaffold. *Science* **338**, 662–665 (2012).
67. Gicking, A. M. *et al.* Kinesin-1, -2, and -3 motors use family-specific mechanochemical strategies to effectively compete with dynein during bidirectional transport. *eLife* **11**, (2022).
68. D'Souza, A. I., Grover, R., Monzon, G. A., Santen, L. & Diez, S. Vesicles driven by dynein and kinesin exhibit directional reversals without external regulators. *BioRxiv* (2022) doi:10.1101/2022.09.27.509758.
69. Belyy, V. *et al.* The mammalian dynein-dynactin complex is a strong opponent to kinesin in a tug-of-war competition. *Nat. Cell Biol.* **18**, 1018–1024 (2016).
70. Elshenawy, M. M. *et al.* Cargo adaptors regulate stepping and force generation of mammalian dynein-dynactin. *Nat. Chem. Biol.* **15**, 1093–1101 (2019).
71. Feng, Q., Gicking, A. M. & Hancock, W. O. Dynactin p150 promotes processive motility of DDB complexes by minimizing diffusional behavior of dynein. *Mol. Biol. Cell* **31**, 782–792 (2020).
72. Qiu, R., Zhang, J. & Xiang, X. Kinesin-1 autoinhibition facilitates the initiation of dynein cargo transport. *J. Cell Biol.* **222**, (2023).
73. Sung, H.-H. *et al.* Drosophila ensconsin promotes productive recruitment of Kinesin-1 to microtubules. *Dev. Cell* **15**, 866–876 (2008).
74. Barlan, K., Lu, W. & Gelfand, V. I. The microtubule-binding protein ensconsin is an essential cofactor of kinesin-1. *Curr. Biol.* **23**, 317–322 (2013).
75. Ferro, L. S. *et al.* Structural and functional insight into regulation of kinesin-1 by microtubule-

associated protein MAP7. *Science* **375**, 326–331 (2022).
76. Hachet, O. & Ephrussi, A. Splicing of oskar RNA in the nucleus is coupled to its cytoplasmic localization. *Nature* **428**, 959–963 (2004).
77. Amrute-Nayak, M. & Bullock, S. L. Single-molecule assays reveal that RNA localization signals regulate dynein-dynactin copy number on individual transcript cargoes. *Nat. Cell Biol.* **14**, 416–423 (2012).
78. Edelstein, A., Amodaj, N., Hoover, K., Vale, R. & Stuurman, N. Computer control of microscopes using µManager. *Curr. Protoc. Mol. Biol.* **Chapter 14**, Unit14.20 (2010).
79. Schindelin, J. *et al.* Fiji: an open-source platform for biological-image analysis. *Nat. Methods* **9**, 676–682 (2012).
80. Sattler, M. Heteronuclear multidimensional NMR experiments for the structure determination of proteins in solution employing pulsed field gradients. *Prog. nucl. magn. reson. spectrosc.* **34**, 93–158 (1999).
81. Simon, B. & Köstler, H. Improving the sensitivity of FT-NMR spectroscopy by apodization weighted sampling. *J. Biomol. NMR* **73**, 155–165 (2019).
82. Delaglio, F. *et al.* NMRPipe: a multidimensional spectral processing system based on UNIX pipes. *J. Biomol. NMR* **6**, 277–293 (1995).
83. Johnson, B. A. & Blevins, R. A. NMR View: A computer program for the visualization and analysis of NMR data. *J. Biomol. NMR* **4**, 603–614 (1994).
84. Williamson, M. P. Using chemical shift perturbation to characterise ligand binding. *Prog. nucl. magn. reson. spectrosc.* **73**, 1–16 (2013).
85. Kieffer, J. *et al.* New data analysis for BioSAXS at the ESRF. *J. Synchrotron Radiat.* **29**, 1318–1328 (2022).
86. Franke, D. *et al.* ATSAS 2.8: a comprehensive data analysis suite for small-angle scattering from macromolecular solutions. *J. Appl. Crystallogr.* **50**, 1212–1225 (2017).
87. Simon, B., Madl, T., Mackereth, C. D., Nilges, M. & Sattler, M. An efficient protocol for NMR-spectroscopy-based structure determination of protein complexes in solution. *Angew. Chem. Int. Ed* **49**, 1967–1970 (2010).
88. Brunger, A. T. Version 1.2 of the Crystallography and NMR system. *Nat. Protoc.* **2**, 2728–2733 (2007).
89. Linge, J. P., Habeck, M., Rieping, W. & Nilges, M. ARIA: automated NOE assignment and NMR structure calculation. *Bioinformatics* **19**, 315–316 (2003).
90. Gruber, A. R., Lorenz, R., Bernhart, S. H., Neuböck, R. & Hofacker, I. L. The Vienna RNA websuite. *Nucleic Acids Res.* **36**, W70-4 (2008).

Supplementary Material

Tropomyosin 1-I/C co-ordinates kinesin-1 and dynein motors during *oskar* mRNA transport

Simone Heber[1†], Mark A. McClintock[2†], Bernd Simon[3], Janosch Hennig[3,4], Simon L. Bullock[2*], Anne Ephrussi[1*]

1 Developmental Biology Unit, European Molecular Biology Laboratory, 69117 Heidelberg, Germany

2 Division of Cell Biology, MRC Laboratory of Molecular Biology, Cambridge CB2 0QH, United Kingdom

3 Structural and Computational Biology Unit, European Molecular Biology Laboratory, 69117 Heidelberg, Germany

4 Biochemistry IV, Biophysical Chemistry, University of Bayreuth, 95447 Bayreuth, Germany

[†]These authors contributed equally to this work

*Correspondence: sbullock@mrc-lmb.cam.ac.uk, anne.ephrussi@embl.org

Supplementary Figures

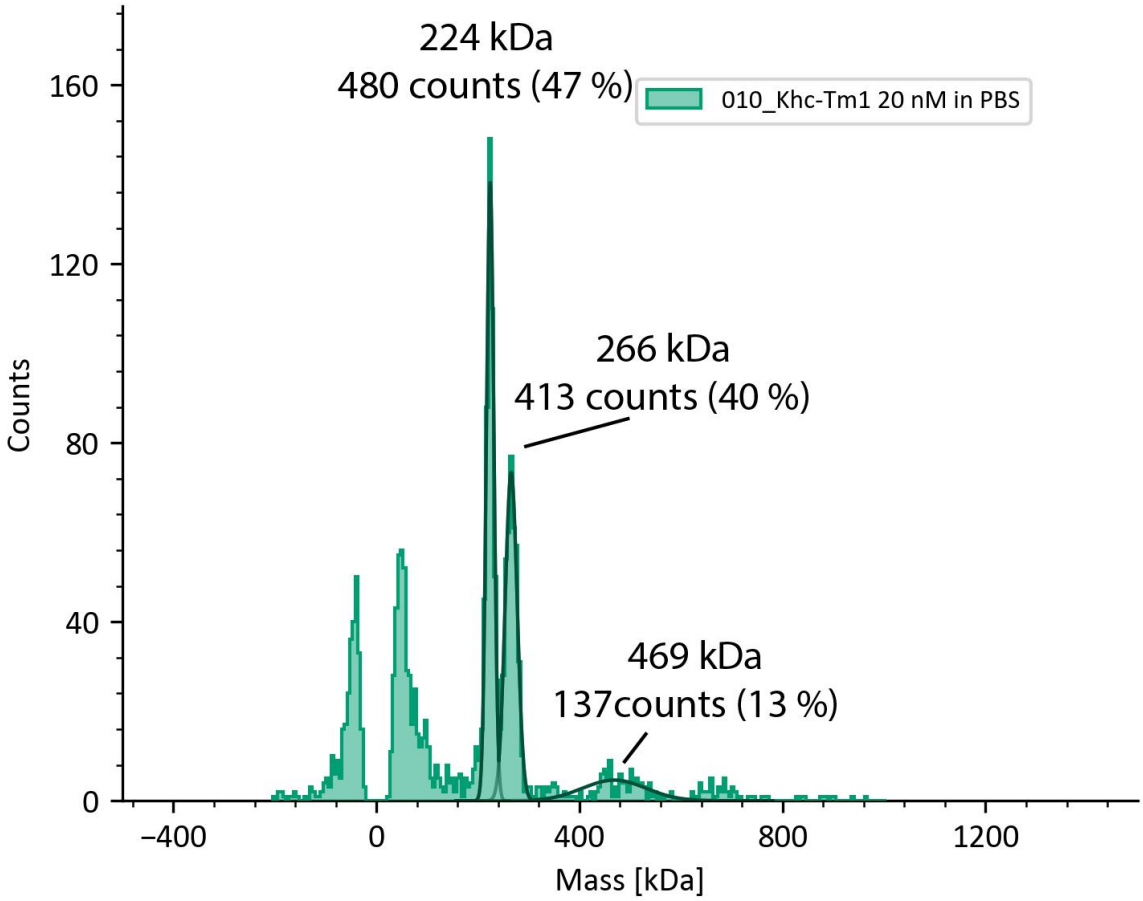

Figure S1: Mass photometry measurements of the Khc-Tm1 complex at 20 nM concentration. The sample comprises a mixture of 47 % particles of 224 kDa, corresponding to the Khc dimer (theoretical MW = 221.2 kDa), 40 % particles of 266 kDa, corresponding to a Khc dimer bound to a Tm1 monomer (theoretical MW = 269.2 kDa), and 13 % of the particles represent larger species. This indicates that in solution, ~50 % of Khc is bound to Tm1 at steady-state at concentrations below the K_D, confirming the 2:1 stoichiometry of the Khc-Tm1 complex[43].

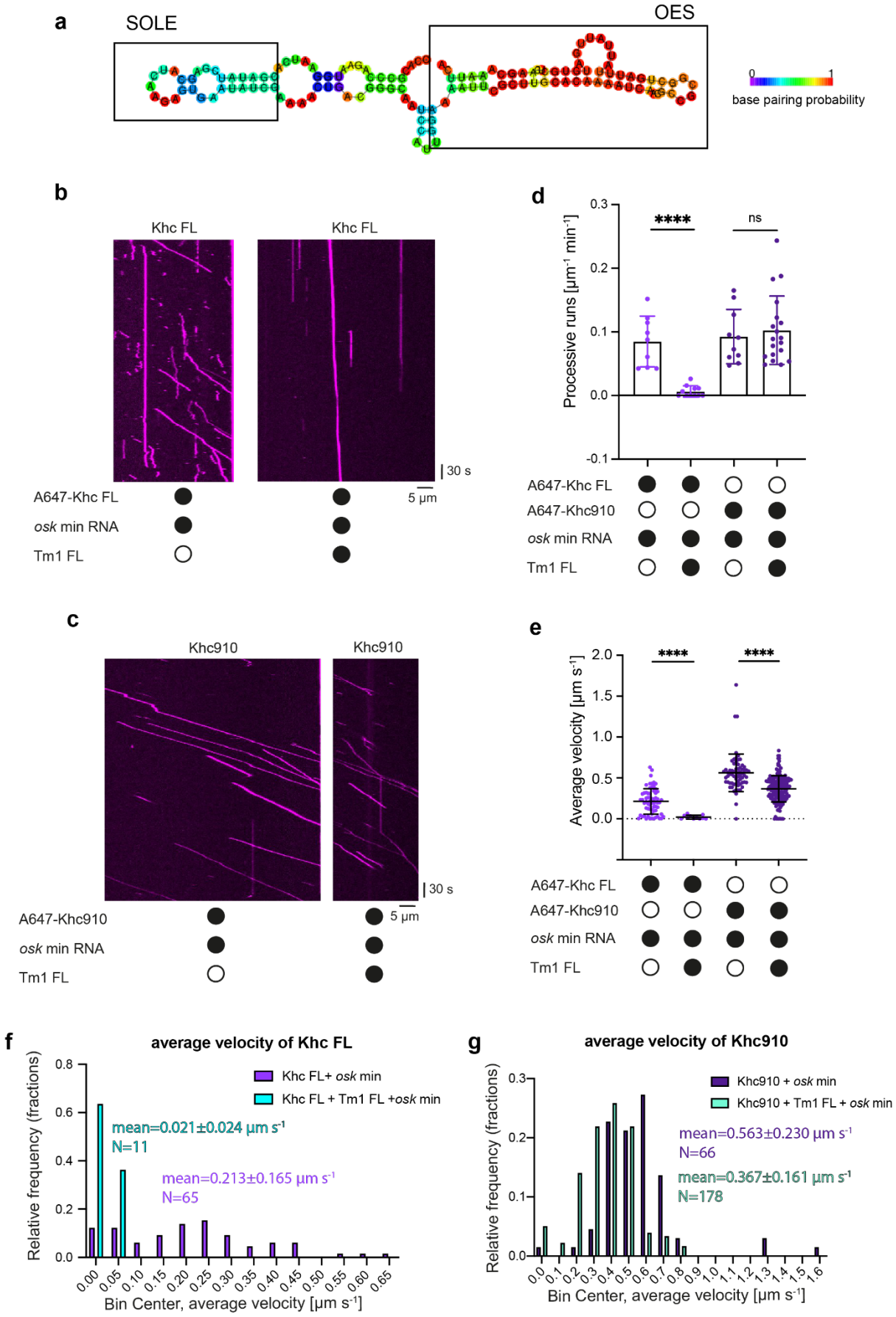

Figure S2: a RNAfold [90] MFE prediction of *osk* min RNA. Both SOLE and OES are predicted as stem-loop structures, indicating that in the context of *osk* min, the LEs adopt their native folds. **b, c** Example kymographs showing processive movements of AlexaFluor647-labeled SNAP-Khc FL (b) or the tailless

Khc910 (c) in absence or presence of Tm1. Microtubule plus and minus ends are oriented toward the right and left of each kymograph, respectively. **d** Processive events of Khc FL and Khc910 in absence or presence of Tm1. In this and other figures, black or white circles indicate proteins that were present or absent from the experiment, respectively. Data points show values for individual microtubules (between 11 and 178 complexes analyzed per condition). Error bars: SD. Statistical significance was evaluated with an unpaired t-test. ****$p<0.0001$. **e** Average velocities of Khc FL and Khc910 in absence or presence of Tm1. Data points represent individual runs. Statistical significance was evaluated with an unpaired t-test. ****$p<0.0001$ **f, g** Histograms of the velocity distributions of Khc FL (f) and Khc910 (g) in absence or presence of Tm1.

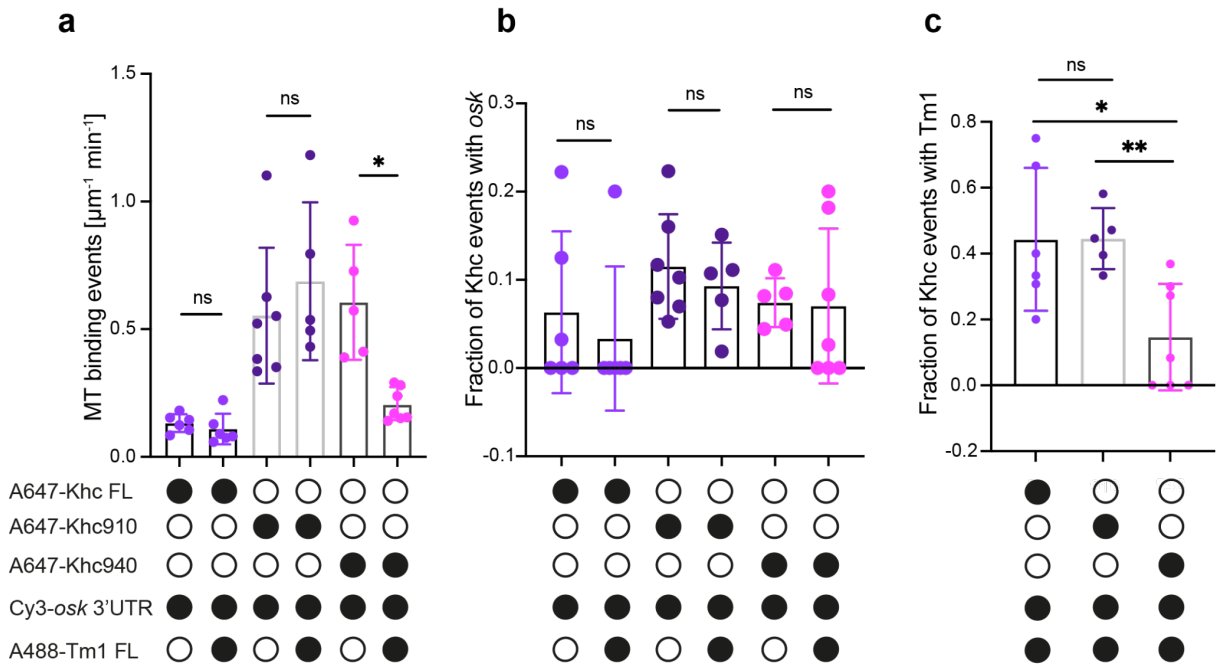

Figure S3: a All microtubule (MT)-binding events (processive, static and diffusive) observed for Khc FL, Khc910 and Khc940 ± Tm1 FL. **b** Fraction of observed Khc events colocalizing with *osk* 3'UTR and **c** fraction of observed Khc events colocalizing with Tm1, for Khc FL, Khc910 and Khc940. Data points show values for individual microtubules. Statistical significance was evaluated with an unpaired t-test. *p<0.1 **p<0.01.

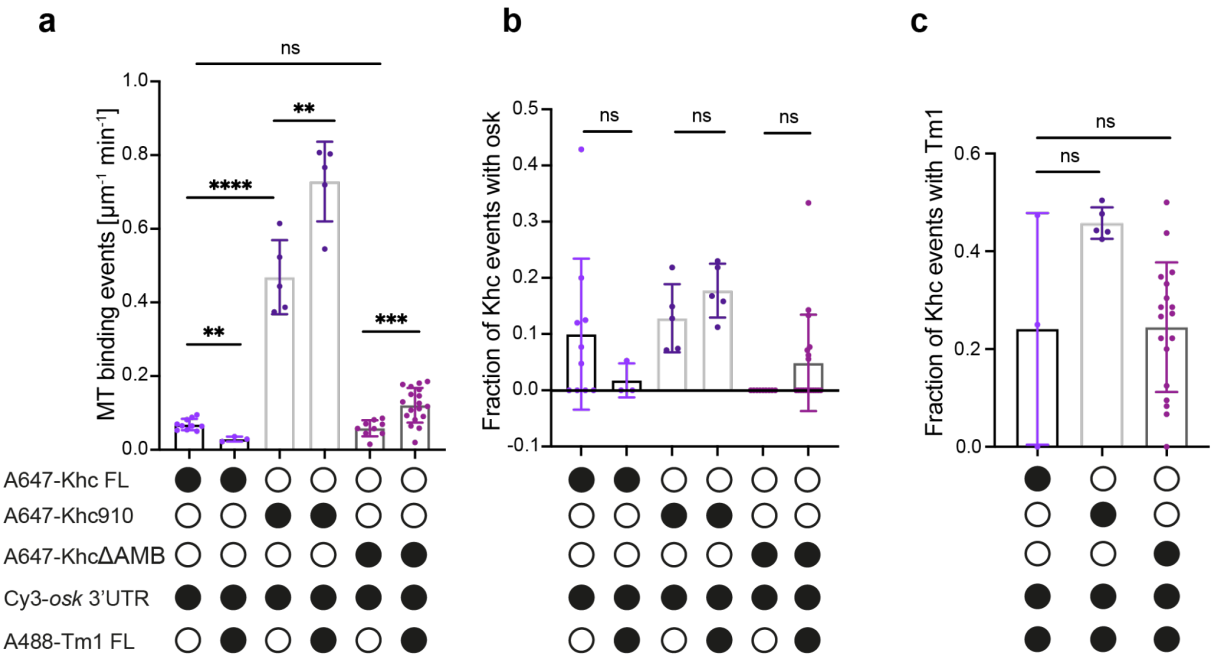

Figure S4: a All microtubule (MT)-binding events (processive, static and diffusive) observed for Khc FL, Khc910 and KhcΔAMB ± Tm1 FL. **b** Fraction of observed Khc events colocalizing with *osk* 3'UTR and **c** fraction of observed Khc events colocalizing with Tm1, for Khc FL, Khc910 and KhcΔAMB. Data points show values for individual microtubules. Statistical significance was evaluated with an unpaired t-test. **p<0.01, ***p<0.001, ****p<0.0001.

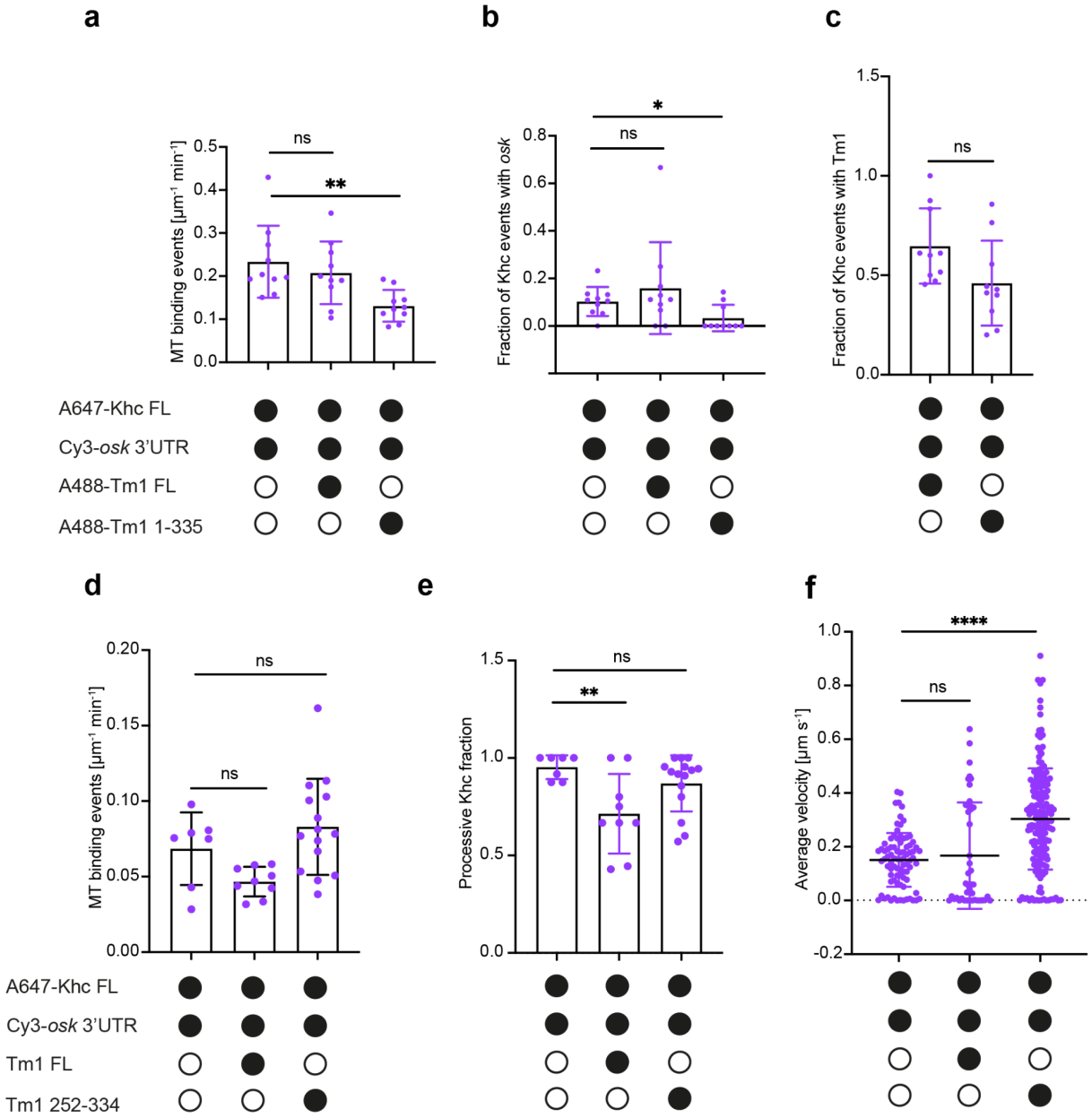

Figure S5: a All microtubule (MT)-binding events (processive, static and diffusive) observed for Khc FL ± Tm1 FL or Tm1 1-335. **b** Fraction of observed Khc events colocalizing with *osk* 3'UTR and **c** fraction of observed Khc events colocalizing Tm1 FL or Tm1 1-335. Labeling efficiencies for Tm1 FL and Tm1 1-335 were 57 %, and 58 %, respectively, such that co-localization results are comparable. **d** All microtubule (MT)-binding events (processive, static and diffusive) observed for Khc FL ± Tm1 FL or Tm1 252-334. **e** Fraction of processive events of Khc FL ± Tm1 FL or Tm1 252-334. **f** Average velocities of Khc FL ± Tm1 FL or Tm1 252-334 in the assembly mix. Data points show values for individual microtubules. Statistical significance was evaluated with an unpaired t-test. *p<0.1 **p<0.01 ****p<0.0001.

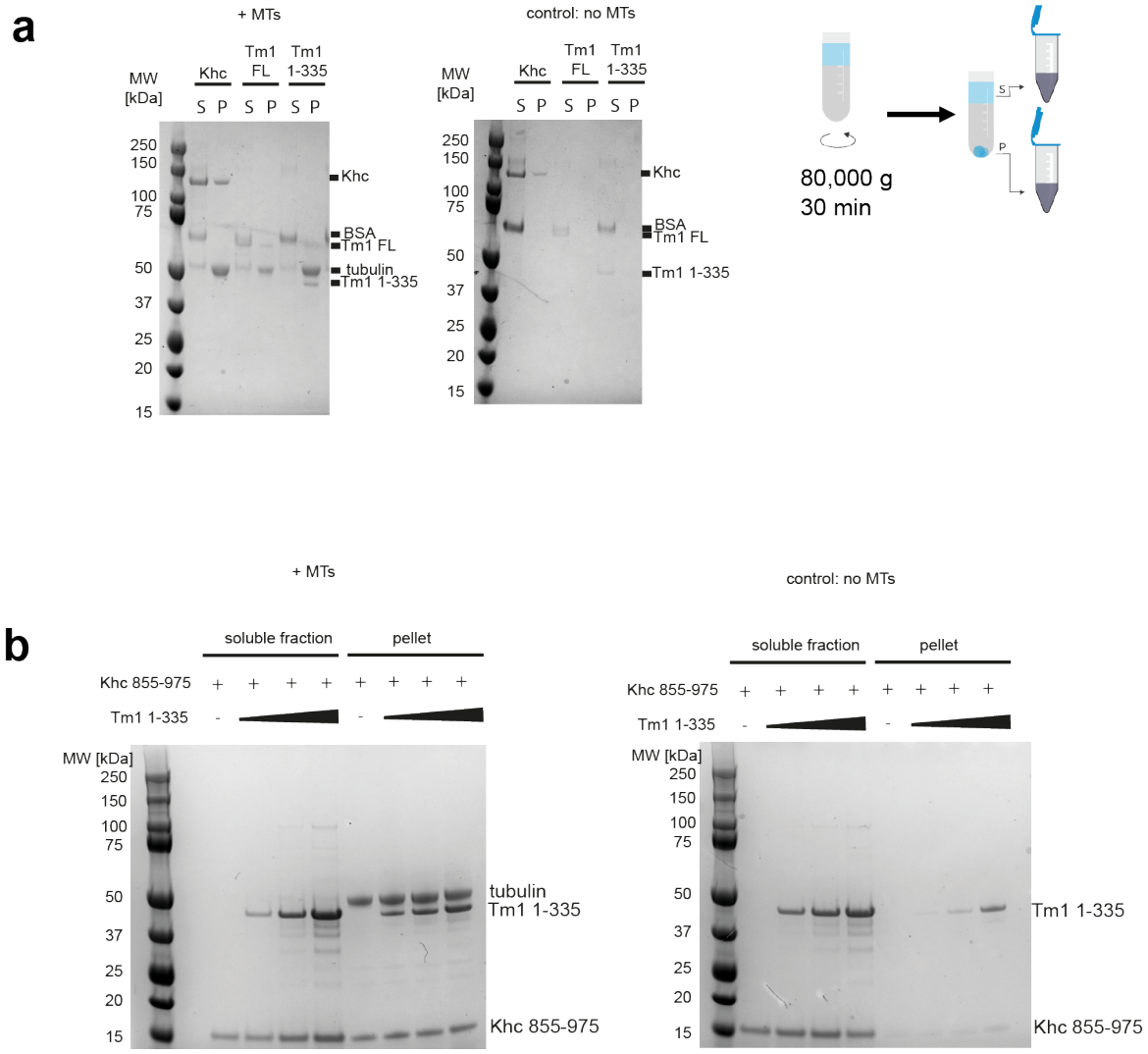

Figure S6: a Microtubule binding assay with Tm1 FL and Tm1 1-335. Khc FL served as a positive control. Both Tm1 FL and Tm1 1-335 partition partially into the microtubule pellet fraction. 10 µg of each protein were incubated with polymerized microtubules prior to segregation of soluble and microtubule-bound fractions by ultracentrifugation over a 30 % sucrose cushion. BSA was added to all samples as a negative control. To control for microtubule-independent pelleting of the proteins, controls without microtubules were performed. Soluble and microtubule pellet fractions were analyzed by SDS-PAGE. **b** Microtubule binding assay with Khc 855-975 and Tm1 1-335. Khc 855-975 partially partitions into the microtubule pellet both in absence and presence of increasing concentrations of Tm1 1-335. 25 µM Khc 855-975 were incubated with Tm1 1-335 at ratios 1:0.5, 1:1 and 1:2 and polymerized microtubules before proceeding as described above.

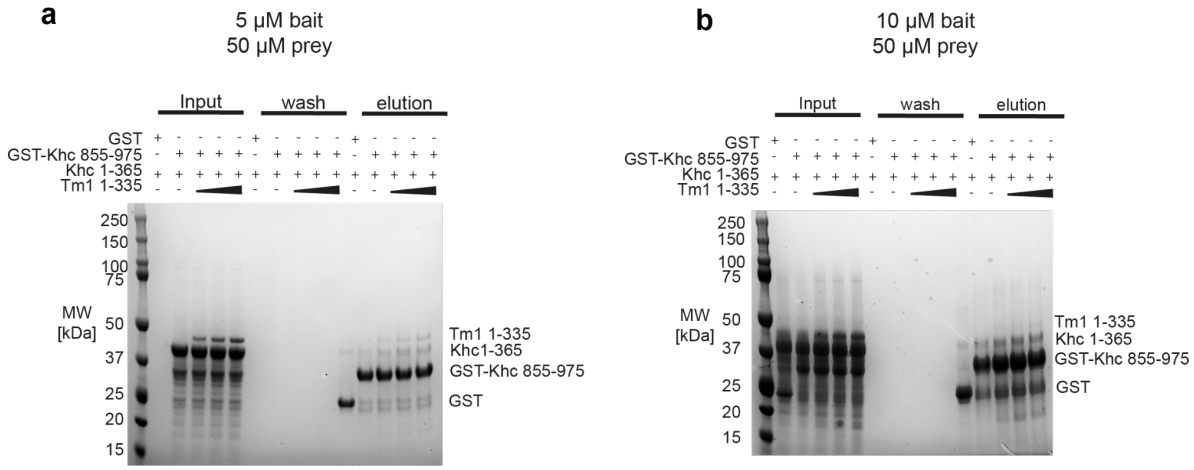

Figure S7: GST-pulldown competition assays to assess the effect of Tm1 on Khc tail - motor interaction. **a** 5 µM or **b** 10 µM GST-Khc 855-975 as bait and 50 µM Khc 1-365 as prey. Tm1 1-335 was added at increasing concentrations (5 to 15 µM) as a competitor for binding to GST-Khc 855-975.

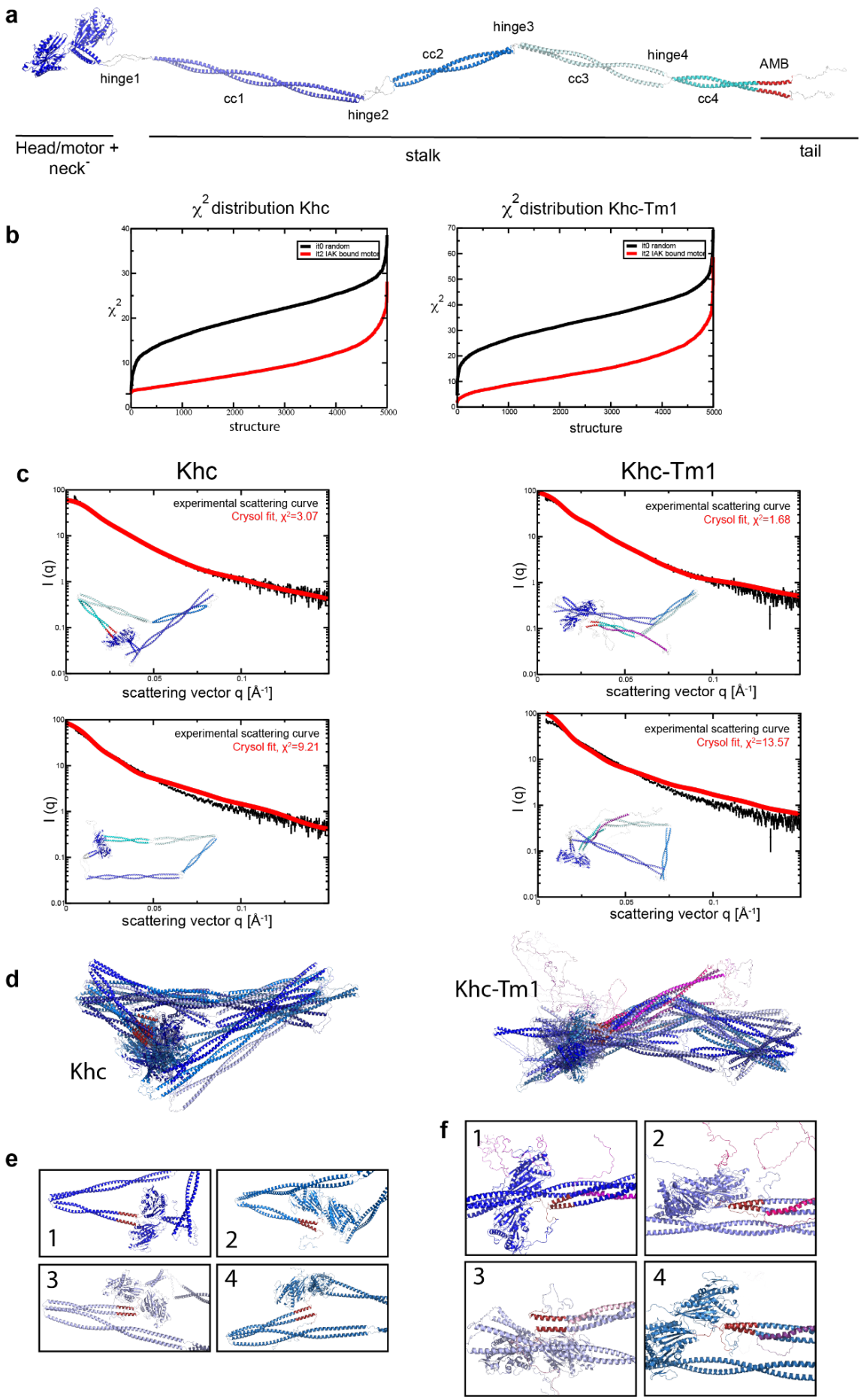
a
hinge1
cc1
hinge2
cc2
hinge3
cc3
hinge4
cc4
AMB
Head/motor + neck
stalk
tail
b
χ2 distribution Khc
χ2 distribution Khc-Tm1
it0 random
it2 IAK bound motor
structure
c
Khc
Khc-Tm1
experimental scattering curve
Crysol fit, χ2=3.07
Crysol fit, χ2=1.68
Crysol fit, χ2=9.21
Crysol fit, χ2=13.57
I (q)
scattering vector q [Å-1]
d
Khc
Khc-Tm1
e
f

1102

Figure S8: **a** Template model of Khc used for randomization. Coordinates of the structured parts (motor domain, residues 1-378 and the four coiled-coil regions, residues 403-585, 604-706, 711-838 and 844-936, respectively) were generated by AF2 [55,56] and connected with the coordinates of the missing linker residues. **b** χ^2 distribution of all Crysol fits to the Khc (left) and Khc-Tm1 (right) scattering curves. **c** Best (upper panel) and mediocre (lower panel) fits of Khc (left) and Khc-Tm1 (right) structural models to the experimental scattering curves. **d** Five best fits for Khc (left) and for Khc-Tm1 (right) aligned. **e** Close-ups of the AMB domains in the four best fitting models for Khc. **f** Close-ups of the AMB domains in the four best fitting models for Khc-Tm1. Khc models are shown in shades of blue with the AMB domains marked in red, Tm1 is shown in shades of pink.

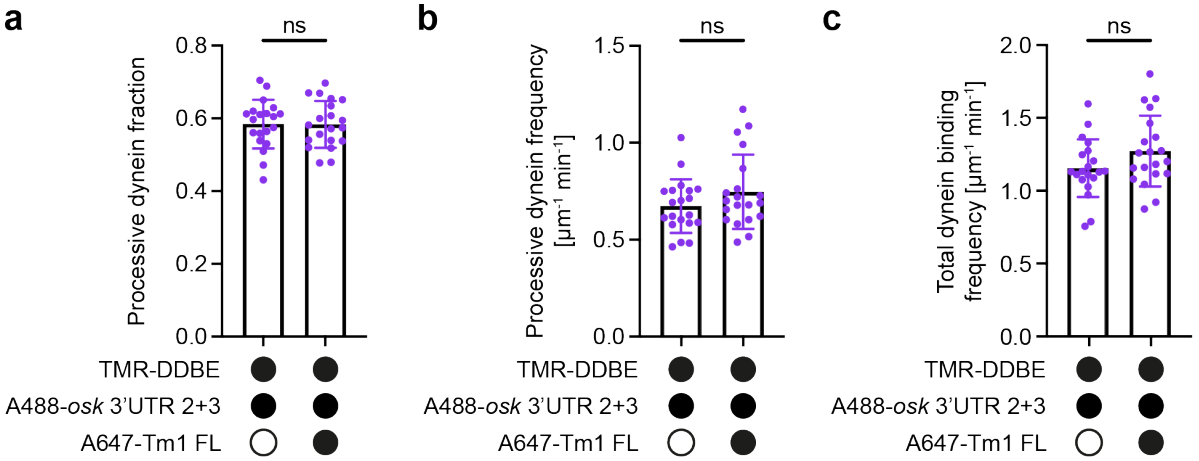

Figure S9: a-c Fraction of dynein binding events that underwent processive motility (a) and frequencies of processive dynein movement (b) and dynein binding to microtubules (c) in the presence and absence of Tm1 FL. Dots represent average values for individual microtubules. In each plot, the mean ± SD is shown. Statistical significance was determined by t-test. ns: not significant.

1118

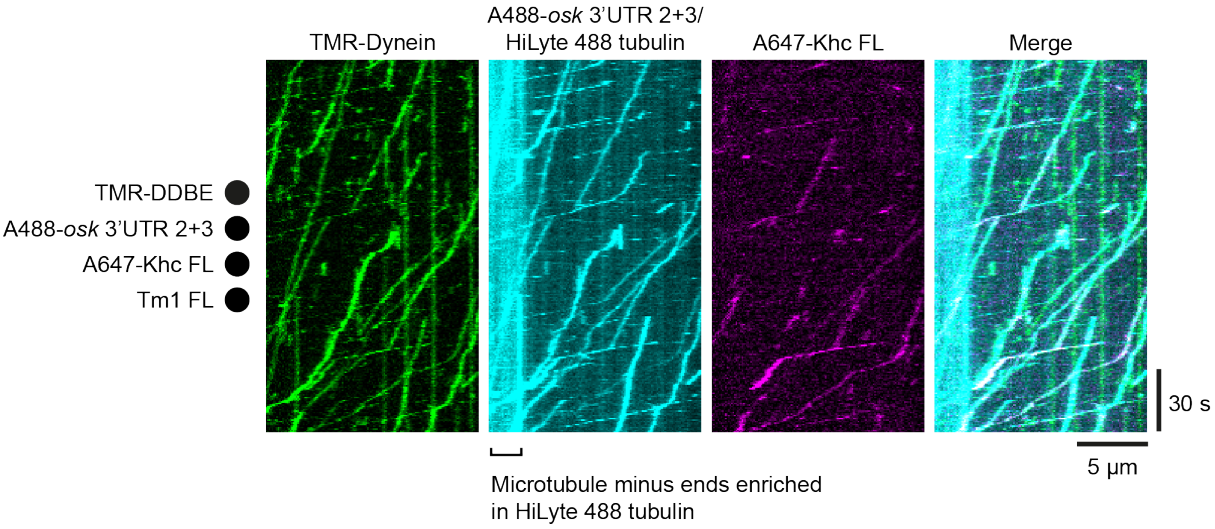

1119

1120 **Figure S10:** Kymographs showing the Tm1-induced co-translocation of dynein, *osk* 3'UTR 2+3 RNA,
1121 and Khc toward microtubule minus ends, which are labeled by enrichment of fluorescent (HiLyte 488)
1122 tubulin dimers. Microtubule plus and minus ends are oriented toward the right and left of each
1123 kymograph, respectively.

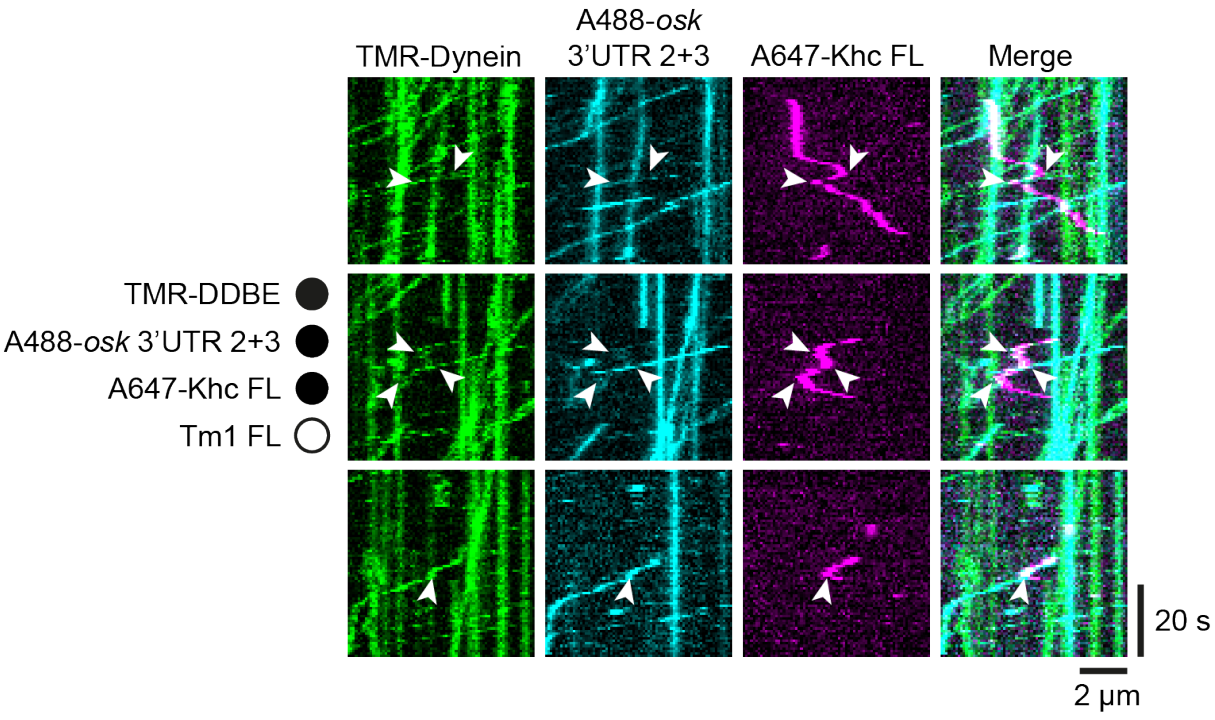

Figure S11: Kymographs showing instances of bidirectional Khc movements in the absence of Tm1. Directional switches of Khc (white arrowheads) correlate with DDBE-*osk* 3'UTR 2+3 association and dissociation events. Microtubule plus and minus ends are oriented toward the right and left of each kymograph, respectively.

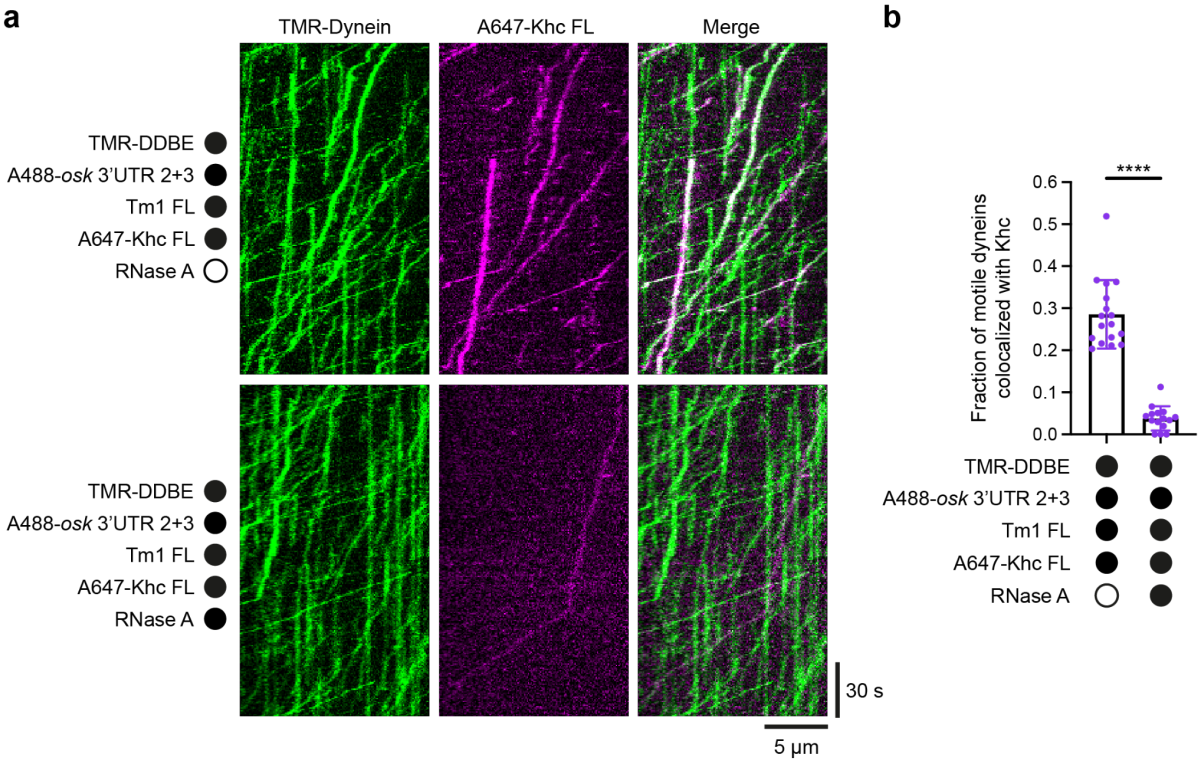

Figure S12: a Kymographs showing reduced association of Khc with motile DDBE-*osk* 3'UTR 2+3 RNPs in the presence of Tm1 after treatment with RNase A. Microtubule plus and minus ends are oriented toward the right and left of each kymograph, respectively. **b** Fraction of moving DDBE-*osk* 3'UTR 2+3 RNPs that colocalized with Khc signal with and without RNase A treatment in the presence of Tm1. Dots represent average values of all motility on individual microtubules. Mean ± SD is shown. Statistical significance was determined by Welch's t-test. ****: $p<0.0001$.

1139 ## Supplementary Tables

1140

	MT binding events [min^{-1} μm^{-1}]	Processive events [min^{-1} μm^{-1}]	Fraction of processive events	Average velocity [μm s^{-1}]
Khc FL N=83	0.13 ± 0.03	0.11 ± 0.03	0.8415	0.183 ± 0.131
+ **Tm1 FL** N=36	0.11 ± 0.06	0.09 ± 0.07	0.8182	0.044 ± 0.422
Khc910 N=438	0.55 ± 0.26	0.55 ± 0.27	1	0.614 ± 0.180
+ **Tm1 FL** N=403	0.68 ± 0.31	0.68 ± 0.31	0.9952	0.560 ± 0.202
Khc940 N=382	0.61 ± 0.23	0.60 ± 0.22	0.9828	0.546 ± 0.260
+ **Tm1 FL** N=97	0.20 ± 0.06	0.15 ± 0.06	0.7327	0.073 ± 0.180

1141 **Table S1** Motility parameters of Khc FL, Khc910 and Khc940

1142

	MT binding events [min^{-1} μm^{-1}]	Processive events [min^{-1} μm^{-1}]	Fraction of processive events	Average velocity [μm s^{-1}]
Khc FL N=142	0.07 ± 0.15	0.05 ± 0.02	0.7696	0.429 ± 0.300
+ **Tm1 FL** N=24	0.02 ± 0.01	0.01 ± 0.01	0.3114	0.159 ± 0.188
Khc910 N=384	0.47 ± 0.10	0.47 ± 0.10	0.8180	0.630 ± 0.169
+ **Tm1 FL** N=595	0.73 ± 0.11	0.72 ± 0.11	0.8955	0.649 ± 0.164
KhcΔAMB N=65	0.06 ± 0.02	0.05 ± 0.02	0.9929	0.507 ± 0.325
+ **Tm1 FL** N=293	0.12 ± 0.05	0.10 ± 0.04	0.9947	0.548 ± 0.266

1143 **Table S2** Motility parameters of KhcΔAMB compared to Khc FL and Khc910

1144

	MT binding events [min^{-1} μm^{-1}]	Processive events [min^{-1} μm^{-1}]	Fraction of processive events	Average velocity [μm s^{-1}]
Khc FL N=335	0.23 ± 0.08	0.16 ± 0.06	0.6847	0.32 ± 0.245
+ **Tm1 FL** N=149	0.21± 0.07	0.09 ± 0.04	0.4449	0.229 ± 0.280
+ **Tm1 1-335** N=170	0.13 ± 0.03	0.06 ± 0.04	0.4376	0.125 ± 0.165
Khc FL N=84	0.07 ± 0.02	0.06 ±0.02	0.9524	0.171 ± 0.212
+ **Tm1 FL** N=44	0.04 ± 0.01	0.03 ± 0.01	0.7137	0.188 ± 0.243
+ **Tm1 252-334** N=171	0.08 ± 0.03	0.07 ± 0.03	0.8694	0.303 ± 0.188

1145 **Table S3** Motility parameters of Khc FL in presence of different Tm1 constructs.

1146

	Total dynein binding frequency [μm^{-1} min^{-1}]	**Processive dynein frequency [μm^{-1} min^{-1}]**	**Processive dynein fraction**	**Average dynein velocity [μm s^{-1}]**	**Average dynein run length [µm]**
DDBE-*osk* 3'UTR 2+3 -Tm1 FL	1.16 ± 0.20 N=20 microtubules (2152 complexes)	0.67 ± 0.14 N=20 microtubules (1277 complexes)	0.58 ± 0.07 N=20 microtubules (2152 complexes)	0.292 ± 0.308 N=1277 complexes	4.26 ± 3.90 N=1277 complexes
DDBE-*osk* 3'UTR 2+3 +Tm1 FL	1.27 ± 0.24 N=20 microtubules (2207 complexes)	0.75 ± 0.19 N=20 microtubules (1295 complexes)	0.58 ± 0.06 N=20 microtubules (2207 complexes)	0.320 ± 0.334 N=1295 complexes	4.25 ± 3.66 N=1295 complexes
DDBE-*osk* 3'UTR 2+3 +Tm1 FL (Tm1-bound only)	N/A	N/A	N/A	0.304 ± 0.310 N=211 complexes	N/A

1147 **Table S4** Motility parameters of DDBE-*osk* 3'UTR 2+3 in presence and absence of Tm1 FL (Related to
1148 Figure 7 and S9). Mean ± SD are shown.

1149

	Frequency of Khc transport events toward plus ends [μm^{-1} min^{-1}]	**Frequency of Khc transport events toward minus ends [μm^{-1} min^{-1}]**	**Average Khc-bound dynein velocity [μm s^{-1}]**	**Average distance traveled by Khc toward minus ends [µm]**
DDBE-*osk* 3'UTR 2+3 +Khc -Tm1 FL	0.005 ± 0.007 N=52 microtubules (29 complexes)	0.014 ± 0.013 N=52 microtubules (89 complexes)	0.236 ± 0.223 N=109 complexes	3.32 ± 3.82 N=109 complexes
DDBE-*osk* 3'UTR 2+3 +Khc +Tm1 FL	0.005 ± 0.008 N=36 microtubules (20 complexes)	0.179 ± 0.064 N=36 microtubules (822 complexes)	0.348 ± 0.281 N=913 complexes	4.92 ± 4.79 N=913 complexes

1150 **Table S5** Motility parameters of DDBE-*osk* 3'UTR 2+3 and Khc in presence and absence of Tm1 FL
1151 (Related to Figure 8). Mean ± SD are shown.

1152 Plasmids

CONSTRUCTS	RELEVANT INFORMATION	SOURCE
pFastBacDual-HisSUMO-SNAP-3C-Khc	Amp^r, p10/Polyhedrin promoter	This study
pFastBacDual-HisSUMO-SNAP-3C-Khc910	Amp^r, p10/Polyhedrin promoter	This study
pFastBacDual-HisSUMO-SNAP-3C-Khc940	Amp^r, p10/Polyhedrin promoter	This study
pFastBacDual-HisSUMO-SNAP-3C-Khc ΔAMB	Amp^r, p10/Polyhedrin promoter	This study
pFastBacDual-HisSUMO-SNAP-3C-Khc-Tm1	Amp^r, p10/Polyhedrin promoter	This study
pGEX6.1-Khc 855-975	Amp^r, tac promoter	This study
pETM11-His6-SUMO-SNAP-Tm1-FL	Kan^r, T7 promoter, lac operator	This study
pETM11-His6-SNAP-SUMO-Tm1 1-335	Kan^r, T7 promoter, lac operator	This study
pETM11-His6-SUMO-Tm1-FL	Kan^r, T7 promoter, lac operator	[43]
pETM11-His6-SUMO-Tm1 1-335	Kan^r, T7 promoter, lac operator	[43]

pETM11-His6-SUMO-Tm1 252-334	Kan^r, T7 promoter, lac operator	43
pDyn1 (pAceBac1-ZZ-TEV-SNAPf-Dynein heavy chain - DYNC1H1)	Gen^r, Polyhedrin promoter	8
pDyn2 (pIDC-Dynein intermediate chain - DYNC1/2, Dynein light intermediate chain - DYNC1LI2, Tctex - DYNLT1, Robl - DYNLRB1, LC8 - DYNLL1)	Chlor^r, Polyhedrin promoter	8
pAceBac1-Egl-TEV-ZZ	Gen^r, Polyhedrin promoter	15
pIDC-BicD	Chlor^r, Polyhedrin promoter	15

Table S6 Plasmids

RNA sequences

***osk* 3'UTR**

GUUGGGUUCUUAAUCAAGAUACAUAUAUGCAAAUUUUGACUGGGCUGGCACC
GGAACCGACAAAAUAAGAACUUUUUGAUGAUUUUACGAUUUACGCUGAUGGA
UCGCUGCUUUUACGGAAUUCGCUUAGUUUUAAUAUGUUUUAUAUGUAGUAUG
UUCUCUGUCUUUGUUUAUUUAUAUGUUCGUGCACUUGUCCUAGUCCAUUAUU
GUAUAUUAUUGUGUGUUUUGUGUUCUAUGUUAGAUUUAAACUUCUCAAUUUU
UCGCUGUCUGUGAUUUGUUUUGCCAAUGCCAUUGAUUUUCUGCACACUUUUU
GCUGCUAUCCCAAAAGCUGUGUAAAAUAAUCAAAUGCAAAAUAAGCGCAAGCA
GCUGAAAACUUCUCUUCAAACUUUUCCGCUUUUCCCAAAACCAUUUUGCUUU
GAAAUCUGUUUUUACCAAAUCAGAUUAAACUGCAAAAUGGAACUUAAAUGCAA
AUCAUUGCAAUGCUUAUAAACUGUUUUUUGUUCUAUAUACUUUUGUGUGGGU
CAAAAUUCGGCAUGCUCCUGUAUCACACAACCUGCCACUUGCCCUUAAAAAG
AAGGGCGCAGUGGGCGUGGUACGUAUACAUAUGAGCCAUGCUGCAUUUUGG
CCGUAAUGAAAAUGCACUGCUUUACUUGGAAAAUUCGCUUGCACAAAAUCAAC
GCCGCGGCUGAUUUAUUAUUGAUGUGCUCAAGCAAAUUCAAGUGAAGCAUUU

GCGCGAUUUUCGUCUUUCUGUUUCCGUUUGCAAAAAAGUUUAUAAAAUGCUU
ACACUCUGCUGCAGACACGCCAACCGGAAGUGCGCACUAAGCGCUUGUUUGU
AGCACAGUGUAGAAUUCUGGCGUAAUUUACAGCUCUACUUUAAAGUCUUCUA
GAUAGCUAUCUACUAUUUAUAAACUUAUUUAUUGUCUUGAAUGUAUGUUAAU
UGUAUGUAUUGAUGGUGAUCACGUUUUUUUUGUCCUAUAACAAGCUGCAAUG
UAAAAUCCAAAAAAAAAAUGAAAAAAUAAAAUAAAAGGGAAAUCAAUGAUUUUG
UUUGCUCUAAGCUAUGUUCAAAGUAACUGG
Total length: 1074 nt

***osk* min**

CCACGCCCAGAAUGGAAUCACGAUAUCGAGCAUCAAGAGUGAAUAUCGAAAA
CUGACGGGCAAUCCAUUGGAAAAUUCGCUUGCACAAAAUCAACGCCGCGGCU
GAUUUAUUAUUGAUGUGCUCAAGCAAAUUCA
Total length: 135 nt
SOLE
OES

***osk* 3'UTR regions 2+3**

UGUUCUAUAUACUUUUGUGUGGGUCAAAAUUCGGCAUGCUCCUGUAUCACAC
AACCUGCCACUUGCCCUUAAAAAGAAGGGCGCAGUGGGCGUGGUACGUAUAC
AUAUGAGCCAUGCUGCAUUUUGGCCGUAAUGAAAAUGCACUGCUUUACUUGG
AAAAUUCGCUUGCACAAAAUCAACGCCGCGGCUGAUUUAUUAUUGAUGUGCU
CAAGCAAAUUCAAGUGAAGCAUUUGCGCGAUUUUCGUCUUUCUGUUUCCGUU
UGCAAAAAAGUUUAUAAAAUGCUUACACUCUGCUGCAGACACGCCAACCGGAA
GUGCGCACUAAGCGCUUGUUUGUAGCACAGUGUAGAAUUCUGGCGUAAUUUA
CAGCUCUACUUUAAAGUCUUCUAGAUAGCUAUCUACUAUUUAUAAACUUAUUU
AUUGUCUUGAAUGUAUGUUAAUUGUAUGUAUUGAUGGUGAUCACGUUUUUUU
UGUCCUAUAACAAGCUGCAAUGUAAAAUCCAAAAAAAAAAUGAAAAAAUAAAAU
AAAAGG
Total length: 530 nt